A scintillator based timing detector for the SHiP experiment

Alexander Dätwyler

supervisors
Prof Nicola Serra, Dr Christopher Betancourt

February 21, 2018

SHiP (Search for Hidden Particles) is a planned fixed target experiment at the Super Proton Synchotron (SPS) at CERN. SHiP's main goal is to detect directly hidden non-Standard Model particles. To exclude one of the main sources of background, the di-muon combinatorial background, a dedicated timing detector with a time resolution less than 100 ps has to be developed and tested.

This study focuses on a timing detector based on plastic scintillating bars with Silicon Photo Multiplier (SiPM) arrays as readout. Timing resolution measurements are compared between set-ups differing in numbers of SiPMs in an array, scintillating plastic material and bar geometry. These results were compared to the 100 ps threshold and are used in design considerations of the final detector.

I have done a terrible thing, I have postulated a particle that cannot be detected.

(Wolfgang Pauli, after postulating the neutrino. — 1930)

Contents

List of Figures

List of Tables

1 Introduction

1.1 Motivation

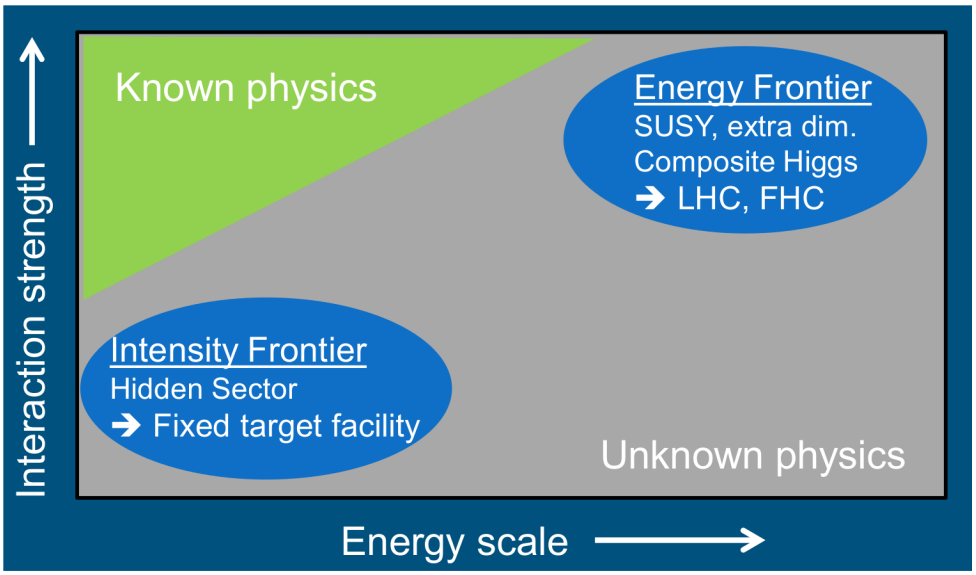

Figure 1.1: The frontiers in particle physics. [1]

The interactions between the elementary particles (leptons, quarks, gauge bosons and the Higgs boson) are described by the Standard Model (SM). This renormalizable model has been tested with a high precision by a multitude of experiments, culminating in 2012 with the discovery of the Higgs boson by the ATLAS [2] and CMS experiments [3]. The Higgs mass of 125 GeV predicts the lifetime for the SM electroweak vacuum that is much longer that the age of the Universe, but the validity of this theory up to the Planck scale has not been yet confirmed [4]. With the measured mass of the Higgs boson, boundaries for several extensions of the SM can be set. These extensions are necessary because the SM can not explain the following phenomena:

- Neutrinos change their flavor by oscillation and have mass
- The Baryon Asymmetry in the Universe (BAU)
- Dark matter, the most abundant kind of matter in the universe
- Cosmological inflation
- Dark energy that drives the acceleration of the expansion of the universe in the present stage

The phenomena can only be described by physics Beyond the SM (BSM), but the observation of new, not yet discovered particles and interactions is needed. New particles may either have a large mass (energy frontier) or have very weak coupling (Intensity frontier) as shown in figure 1.1. SHiP (Search for Hidden Particles) is a proposed experiment to search for new weakly interacting particles in the intensity frontier.

1.2 Physics

There are mainly three types of portals studied in SHiP [1]:

- **Vector Portal:** New abelian vector fields mixing with the photon and the Z^0.
- **Scalar Portal:** neutral singlet scalar particles coupling to the Higgs field.
- **Neutrino Portal:** new neutral singlet leptons coupling to the singlet operators of the SM.

All three portals are predicted naturally by theories beyond the Standard Model (BSM) and are renormalizable in the SM.

1.2.1 The Dark Photon of the Vector Portal

If the SM descends from any Grand Unified Theory (GUT) or any other larger gauge group, then the SM could include additional gauge symmetries, like multiple $U(1)$s which would give the SM a $SU(3) \times SU(2) \times \{(U(1)\}^n$ structure. If these $U(1)$ have relatively light vector states and small couplings to the SM, then they would be hardly measurable in the LHC experiments and would therefore be an attractive goal for any intensity frontier experiment such as SHiP. [1]

Several models that include dark matter predict the existence of a hidden sector of particles that are singlet under the SM gauge group. These particles are neutral, have not been observed and can only interact with the SM particles via a "messenger" particle which belongs to the hidden sector. The simplest QED-like models consist of a $U(1)'$ gauge symmetry in the hidden sector, whose gauge boson γ' is called the dark photon. If $U(1)'$ is broken by a Higgs-like mechanism, then the dark photon is massive.

The SM Lagrangian can be extended to:

$$\mathcal{L} = \mathcal{L}_{SM} + \mathcal{L}_{QED(A')} + \frac{\epsilon}{2} \cdot F'_{\mu\nu} F^{\mu\nu} \frac{m^2_{\gamma'}}{2} \cdot A'_\mu A'^\mu, \tag{1.1}$$

where

- $\mathcal{L}_{SM}$ is the SM Lagrangian
- $\mathcal{L}_{QED(A')}$ is the QED-like Lagrangian of the hidden sector, charged under $U(1)'$
- A_μ is the SM gauge field of the $U(1)$ group
- $F_{\mu\nu} \equiv \partial_\mu A_\nu - \partial_\nu A_\mu$
- A'_μ is the new gauge field of the $U(1)'$ group
- $F'_{\mu\nu} \equiv \partial_\mu A'_\nu - \partial_\nu A'_\mu$
- ϵ is the coupling strength between the SM and the hidden sector

The additional terms of the Lagrangian are

- $\frac{\epsilon}{2} \cdot F'_{\mu\nu} F^{\mu\nu}$ is the kinetic mixing between the new gauge field and the SM
- $\frac{m^2_{\gamma'}}{2} \cdot A'_\mu A'^\mu$ is the mass term for γ'

The dark photon might be found in neutral di-leptonic and di-hadronic final states if the γ' mixes with the SM through loops of particles charged under $U(1)$ and $U(1)'$. Assuming γ' is the lightest particle of the hidden sector, it would decay into $l^- l^+$ or $q\bar{q}$ final states via a virtual photon. In case of a decay into $l^- l^+$ and $q\bar{q}$, the partial decay width is given by:

$$\Gamma(\gamma' \to l^- l^+) = \frac{1}{3} \alpha_{QED} m_{\gamma'} \epsilon^2 \cdot \sqrt{1 - \frac{2m_l^2}{m^2_{\gamma'}}} \cdot \left(1 + \frac{4m_l^2}{m^2_{\gamma'}}\right) \tag{1.2}$$

$$\Gamma(\gamma' \to q\bar{q}) = \frac{1}{3} \alpha_{QED} m_{\gamma'} \epsilon^2 \cdot R(m_{\gamma'}) \tag{1.3}$$

$$\text{where } R(\sqrt{s}) = \frac{\sigma(e^+e^- \to hadrons)}{\sigma(e^+e^- \to \mu^+\mu^-)}, \tag{1.4}$$

where $R(\sqrt{s})$ is the energy dependant ratio of the cross section σ quantifying the hadronic annihilation in e^+e^- collisions, m_l is the mass of the lepton and α_{QED} is the fine structure

constant of QED. Another source of the dark photon can be found in bremsstrahlung, as shown in figure 1.2. [5]

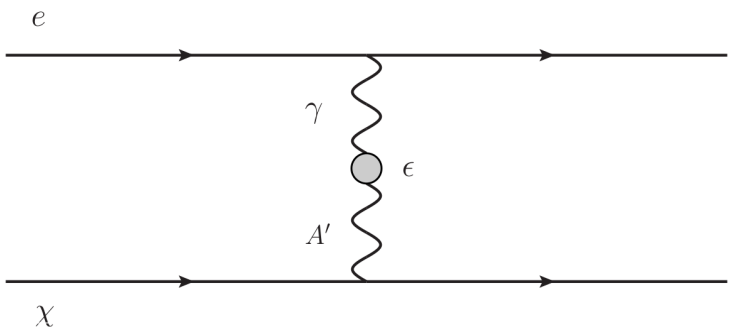

Figure 1.2: Interaction between the SM particle e and hidden sector particle χ, which is charged under $U(1)'$ group, is possible through a mixed $\gamma - \gamma'$ propagator. [1]

In recent years, a number of experimental studies already have explored the parameter space of the dark photon via the vector portal. A summary of the already excluded phase space and the accessible region for SHiP are shown in figure 1.3.

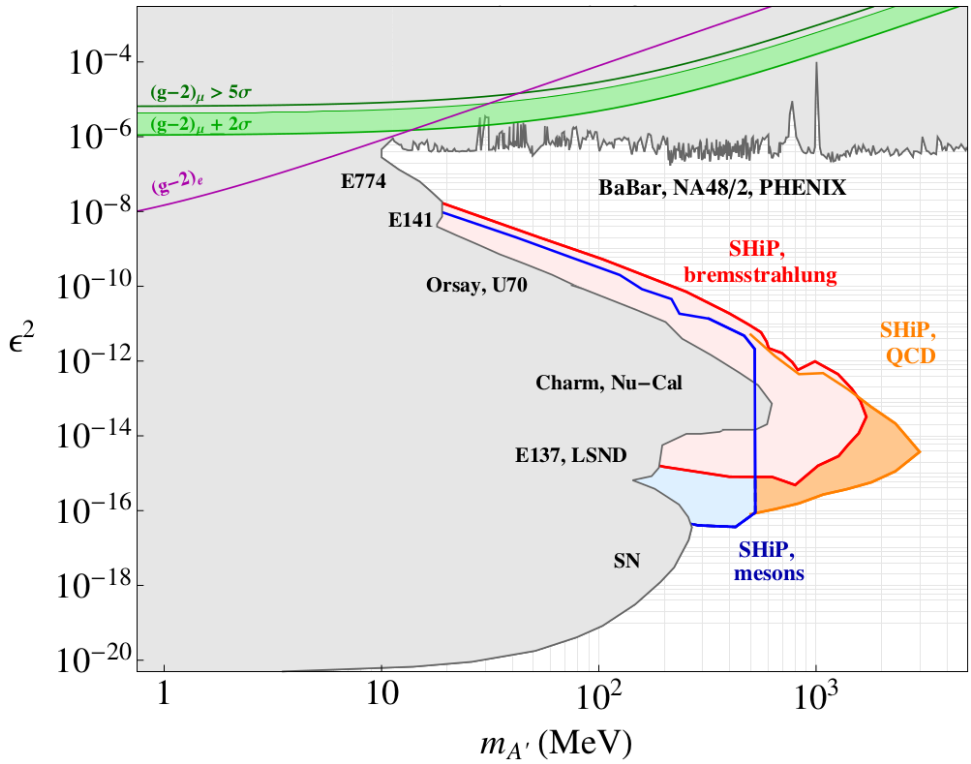

Figure 1.3: Sensitivity of SHiP to γ' with mass $m_{\gamma'}$ versus coupling strength ϵ produced in proton bremsstrahlung (red), secondary meson decay (blue) and by direct QCD interaction (orange). The area excluded by previous experiments is greyed-out. [1]

1.2.2 The light scalar particle mixing with the Higgs field: the Scalar Portal

Various extensions of the SM require the existence of additional scalar fields. For example, the large difference between the weak force and gravitation (hierarchy problem) can be explained by the introduction by a new scalar field [6]. The SHiP experiment has is a potential way to probe the scalar potential, provided that the particles connected to it have the masses of $\mathcal{O}(\mathrm{GeV/c^2})$[7].

Those models who predict the existence of light inflation have a term in the Lagrangian which couples the Higgs field Φ to a neutral singlet scalar singlet S_i through the scalar potential:

$$\mathcal{L}_S P = (\lambda_i S_i + g_i S_i)(\Phi^\dagger \Phi) \tag{1.5}$$

where the λ_i are the dimensionless and g_i are the dimensionfull couplings.

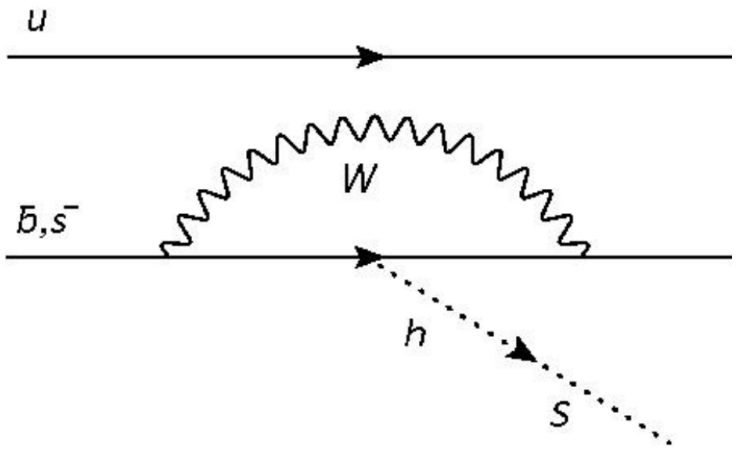

Figure 1.4: Main diagram of light scalar production in meson decay through mixing of virtual Higgs h, e.g. $B^+ \to K^+ S$. [7]

The extra real singlet scalar couples to the Higgs field via a constant mixing term $sin^2\theta$. Therefor the production of it is linked to the production of the Higgs boson (mass $\approx 125\,\text{GeV}$). The production of a light scalar S via the decay of a B^+ meson (mass $\approx 5.3\,\text{GeV}$) to a K^+ (mass $\approx 0.5\,\text{GeV}$) through mixing of a virtual Higgs H^*, $B^+ \to K^+ S$, is shown in figure 1.4. The mixing of the different eigenstates can be expressed by a mixing matrix:

$$\begin{pmatrix} |H'\rangle \\ |S'\rangle \end{pmatrix} = \begin{pmatrix} \cos\theta & \sin\theta \\ -\sin\theta & \cos\theta \end{pmatrix} \begin{pmatrix} |H\rangle \\ |S\rangle \end{pmatrix} \tag{1.6}$$

$$\Rightarrow |H'\rangle = \cos\theta |H\rangle + \sin\theta |S\rangle \tag{1.7}$$

The mixing angle $\sin\theta$ expresses the probability of a virtual Higgs producing an scalar S. If no lighter scalar exist, it will decay into SM particles. These SM particles will be either leptons, mesons or photon pairs, depending on the mass of the S. The decay width for the leptons is:

$$\Gamma(S \to l\bar{l}) = \frac{\sin^2(\theta) m_l^2 m_S}{8\pi\nu^2} \left(1 - \frac{4m_l^2}{m_S^2}\right)^{\frac{3}{2}} \tag{1.8}$$

where m_S and m_l are the masses of the scalar singlet and lepton, and ν is the electroweak vacuum expetation value. The sensitivity contours of the SHiP for light scalar particle mixing with Higgs is shown in figure 1.5.

1.2.3 The Neutrino Minimal Standard model (νMSM): Neutrino Portal

The Neutrino Minimal Standard Modell (νMSM) is a minimalistic extension of the SM that adds three Heavy Neutral Leptons (HNLs) as shown in figure 1.6. The νMSM is an attempt to explain neutrino masses, dark matter and the matter-antimatter asymmetry observed in the Universe without any new physics between the Fermi and Planck scale. HNL states are $SU(2) \times U(1)$ singlets and don't interact electroweakly. They are also known as sterile neutrinos [5]. The extended Lagrangian $\mathcal{L}$ for the νMSM is:

$$\mathcal{L} = \mathcal{L}_{SM} + \bar{N}_i i\partial\!\!\!/ N_i - U_{i\alpha}\Phi\bar{N}_i L_\alpha - \frac{M_i}{2}\bar{N}_i^c N_i + h.c. \tag{1.9}$$

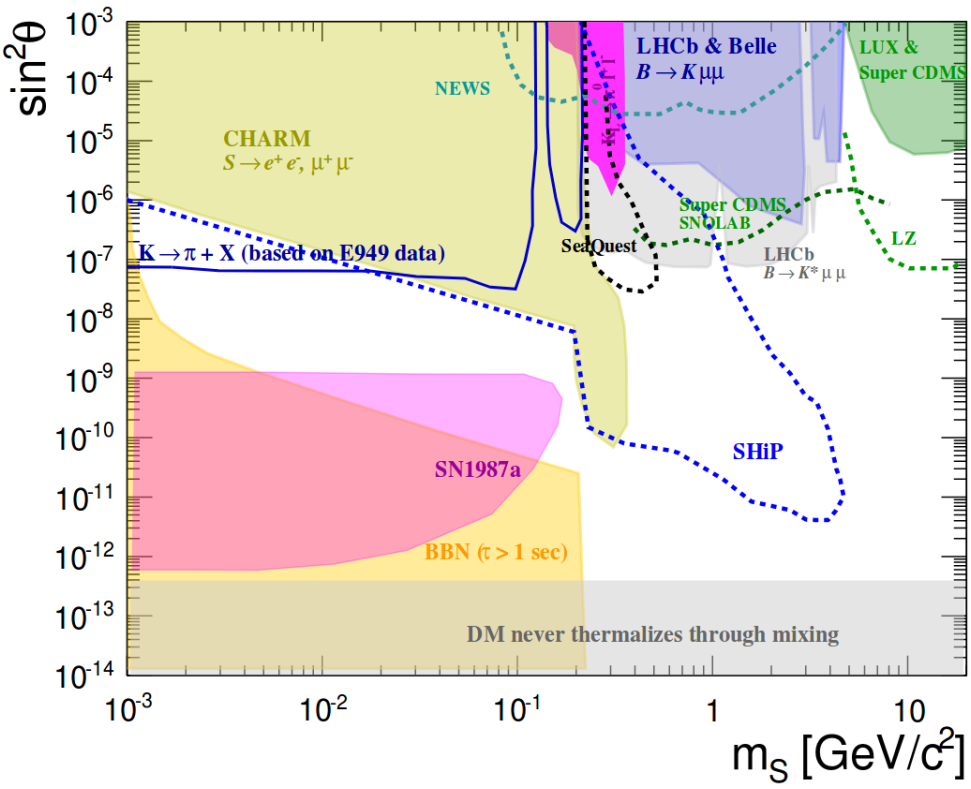

Figure 1.5: The sensitivity contours for light scalar particles mixing with a Higgs, scalar mass m_S versus coupling strength $sin^2\theta$. The SHiP sensitivity correspond to the blue dotted line, the other dotted lines represent the sensitivity of other planned experiments. The shaded areas are parameter regions excluded by past experiments. [7]

with

- $\mathcal{L}_{SM}$: The SM Lagrangian
- N_i: The sterile neutrino fields
- Φ: The Higgs doublet $\tilde{\Phi}_a = \epsilon_{ab}\Phi_b$
- L_α: The left handed doublet
- U: the matrix for the Yukawa couplings (Dirac mass)
- M_i: A Majorana mass

Only the right handed part of the N_i couple to the SM sector. The Majorana masses are assumed to be of the order of the electroweak scale or below in this model and, to be consistent with neutrino experiments, the Yukawa couplings must be very small:

$$U_i^2 \sim \mathcal{O}\left(\frac{m_\nu M_i}{\nu^2}\right) \tag{1.10}$$

where m_ν are the neutrino masses and and ν is the vacuum expetation value of the Higgs field.

N_1 is a dark matter candidate with a lifetime greater than the age of the Universe, it has a mass of $\mathcal{O}$(keV). N_1 and N_2 have a mass of $\mathcal{O}$(keV to GeV) and their mass is degenerate. Through the hypothetical process leptogenesis they create a lepton-antilepton asymmetry in the universe.

In this model leptogenesis arises due to right handed neutrionos without SM gauge interactions, which can therefor have a Majorana mass, and violates lepton number (see seesaw mechanism). The two heavier sterile neutrinos could explain the observed pattern and the smallness of the masses of the left handed neutrinos. Other models beyond the νMSM predict the existence of right handed neutrinos with Majorana mass. The coexistence of Majorana masses are important

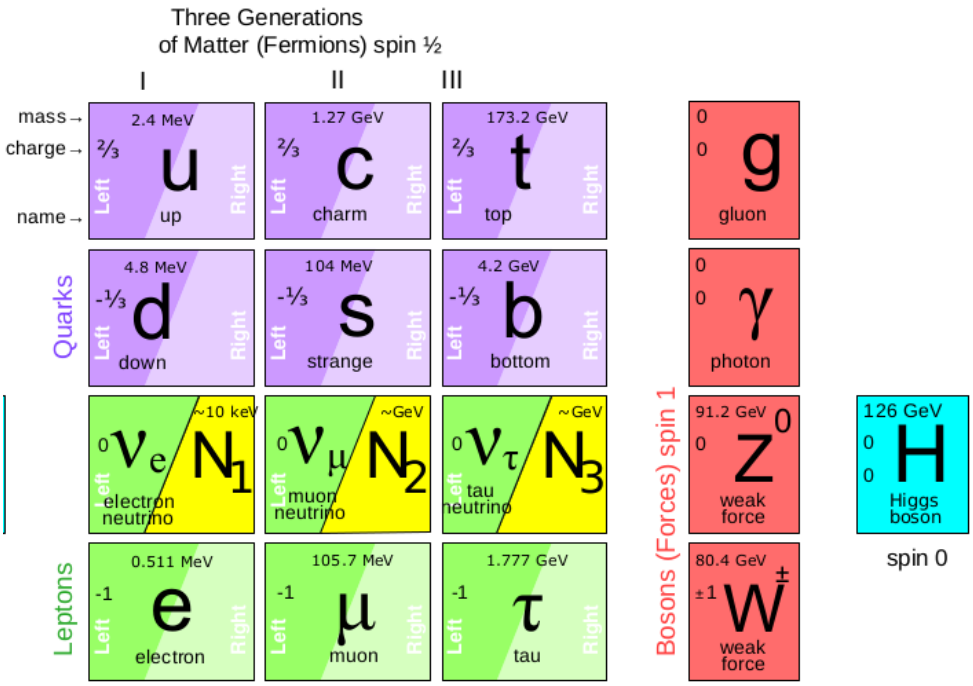

Figure 1.6: The νMSM adds three particles (N_1, N_2 and N_3) to the SM. They are right-handed counterparts to the neutrinos and do not interact weakly, electromagnetically nor strongly. [8]

elements of GUTs.

The production of sterile neutrinos is described in source [9]. HNLs can be produced by kinetic mixing of an SM neutrino. The decay is the reversal of the process, the HNL again mixes with an SM neutrino, can be seen in figure1.7.

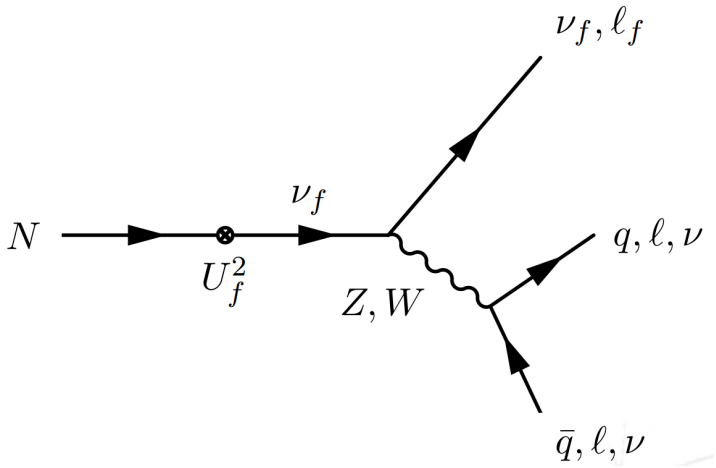

Figure 1.7: The decay of a HNL through mixing with a SM neutrino. Massive neutrinos can decay through the emission of a Z^0 or a $W^{\pm}$ into different final states. [5]

Seesaw Mechanism The simplest seesaw mechanism produces one of the three known neutrinos and a corresponding very heavy neutrinos. These very heavy neutrinos have not been observed yet.

The neutrino mass term of the Lagrangian $\mathcal{L}$ can be expressed as:

$$\mathcal{L}_{m_\nu} = -\frac{1}{2}\begin{pmatrix}\bar{\nu}_L & \bar{\nu}_R^c\end{pmatrix}\mathcal{A}\begin{pmatrix}\nu_L^c \\ \nu_R\end{pmatrix} + h.c. \tag{1.11}$$

where ν_L and ν_R are the left and right handed neutrinos. $\mathcal{A}$ is a 2x2 matrix containing the Majorana mass $m$and Dirac mass M, and it has following structure:

$$\mathcal{A} = \begin{pmatrix} 0 & m \\ m & M \end{pmatrix} \tag{1.12}$$

The two eigenvalues of $\mathcal{A}$ are:

$$\lambda_{\pm} = \frac{M \pm \sqrt{M^2 + 4m^2}}{2} \tag{1.13}$$

$$\text{assuming } m \ll M \tag{1.14}$$

$$\lambda_{+} \approx M \tag{1.15}$$

$$\lambda_{-} \approx -\frac{m^2}{M} \tag{1.16}$$

If one of the $\lambda_{\pm}$ becomes larger, the other one gets smaller, that's why this mechanism got the name "seesaw". From equation 1.11 we get the Dirac and Majorana mass terms

$$m_D = m(\bar{\nu}_L \nu_R + \bar{\nu}_R \nu_L) \tag{1.17}$$

$$m_M = \frac{1}{2} M(\bar{\nu}_R \nu_R^c + \bar{\nu}_R^c \nu_R) \tag{1.18}$$

The seesaw mechanism gives explanations to several problems:

- The small λ_- from equation 1.16 can produce a very small neutrino mass $\sim 1\,\text{eV}$, which is in agreement with experiments, it can also explain why the observed neutrino mass is much smaller than the mass of the other leptons and quarks.
- If the Majorana mass component M is equal to λ_+ from equation 1.15 it can be comparable to the GUT scale, while the Dirac masses are of the much smaller electroweak order .
- From equation 1.18 can be concluded that the Majorana mass term violates the lepton number. Two neutrinos can be created from vacuum ($n_l = 0 \rightarrow n_l = 2$)or neutrinos can be destroyed without the creation of any new leptons. The weak charge is therefor also not conserved.

Simple models with HNLs have four free parameters:

- Three mixing paramters U_e^2, U_μ^2 and U_τ^2
- The HNL mass m_N

Usually the sum of all free parameters as the total coupling to the SM U^2 is used to present results. Since only the general relationships of these couplings is known, without identification, there are 5 hierarchy scenarios. In figure 1.8, the sensitivity contours in the parameter space for the νMSM of the so called normal hierarchy is shown. The normal hierarchy follows:

$$U_e^2 : U_\mu^2 : U_\tau^2 \approx 1 : 16 : 3.8 \tag{1.19}$$

The interpretation of the limits in this parameter space therefor only depends on the active neutrino masses and the total coupling U^2 is varied over the parameter scale.

1.3 SHiP (Search for Hidden Particles)

The SHiP experiment is a proposed at the CERN SPS accelerator. A proton beam with an energy of 400 GeV will be dumped on a heavy target to produce $2 \cdot 10^{20}$ proton-target interaction over five years. It is suggested to implement SHiP with minimal modification on the SPS complex

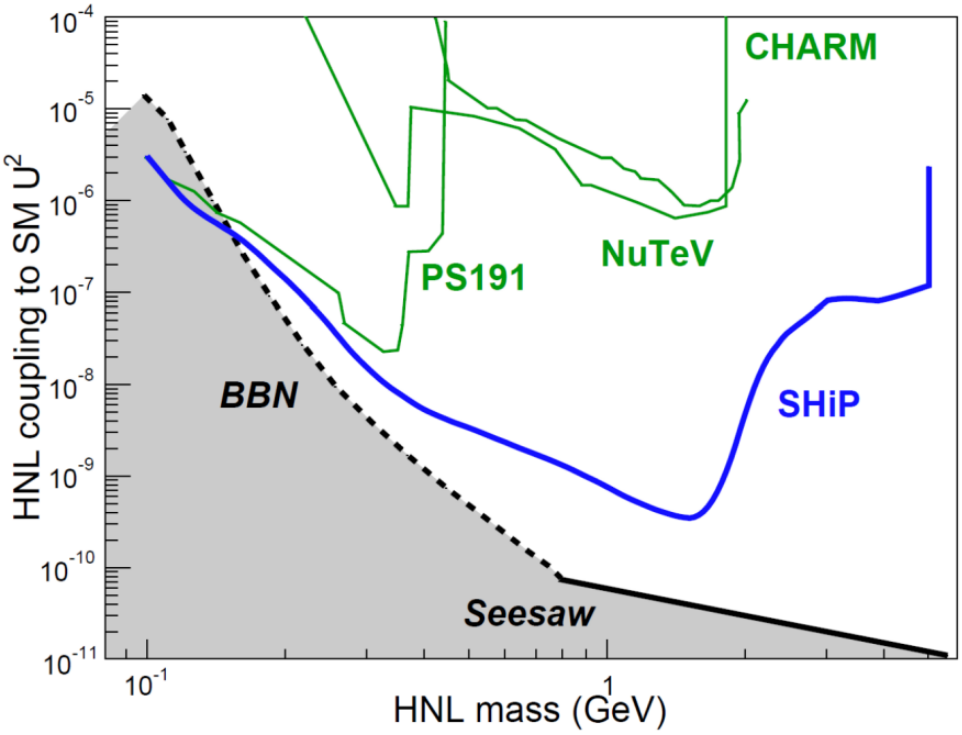

Figure 1.8: Sensitivity contours for HNL coupling to active neutrino as function of HNL mass. [10]

and using existing transfer lines as much as possible. The position of the SHiP facility in the CERN Prevesin site can be seen in figure 1.9.

The SHiP collaboration has submitted a technical proposal [10] and a physics paper [1] in April 2015. The SPS and PS experiments Committee (SPSC) recommended the SHiP collaboration to submit a comprehensive design study [12]. The collaboration is now in the process of developing, testing and refining all aspect of the project and plans to start to take data in 2026, if the experiment is approved in 2021.

1.3.1 SHiP Setup

The following is a short description of the SHiP experiment and each subdetector. The entire experiment is illustrated in figure 1.10.

1) Target The target on which the 400 GeV proton beam will be dumped on must consist of a material with the shortest possible nuclear interaction length to maximize the production of heavy mesons and minimize the production of neutrinos and muons. Furthermore, it has to minimize the flight of pions and kaons. Therefore the target will be composed of 13 titanium-zirconium doped molybdenum blocks followed by 5 tungsten blocks. These blocks either are of rectangular shape (30 cm × 30 cm) or cylindrical with 25 cm diameter. Either way, the total length of the target will be about 150 cm All watercooled blocks will be cladded with Thallium. [13]

2) Muon magnetic shield The reduction of the μ flux is of great importance, it represents the main background source due to $\sim 5 \cdot 10^9$ μ per spill produced by the p-collisions in the target. The design of the shield strongly depends on the spectrum of the μ, which has been predicted by simulations.

[1]The numbers correspond to to the numbers in the paragraphs below. The schematic of the SHiP experiment are provided by Iaroslava Bezshyiko.

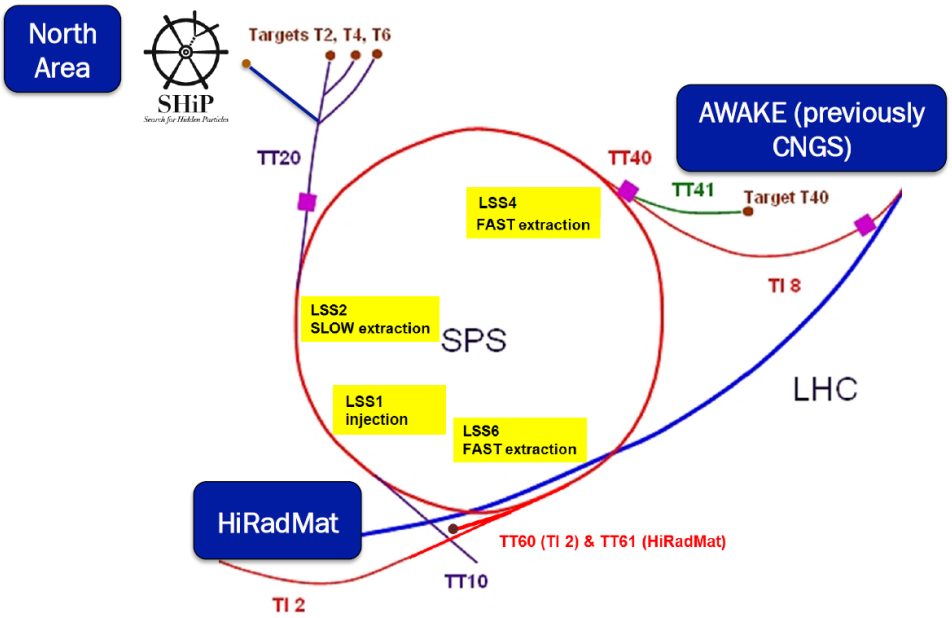

Figure 1.9: Overwiew of the SPS accelerator complex at CERN. SHiP will be located at the north area and shares the TT20 transfer line with other fixed target programs. [11]

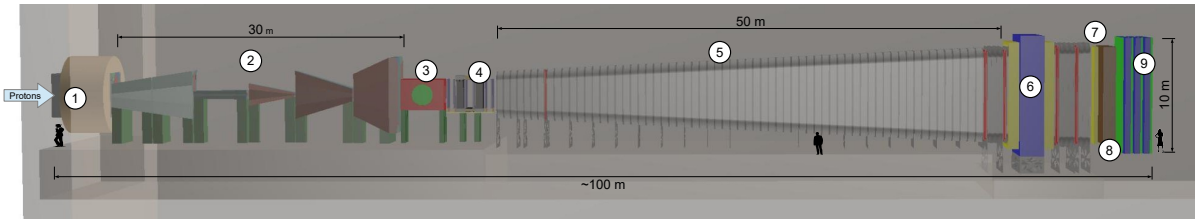

Figure 1.10: The SHiP experiment. 1)Target, 2)Muon magnetic Shield, 3)ν_τ Detector, 4)Muon Magnetic Spectrometer, 5)Hidden Sector Decay Volume, 6)Spectrometer 7)Veto Timing Detector,8)Calorimeter ,9)Muon Detector. [1]

Muons with an energy of 350 GeV have to be bent out of the 5 m aperture of the Vacuum vessel, requiring a total field strength of $B_y = 40$ Tm. The major challenges for the shield are the return fields of long sequences of magnets, which bend the muons back towards the detector, and backscattering on the experimental hall. [14]

3) ν_τ Detector The main motivation of the ν_τ-detector is the first direct observation of the $\overline{\nu}_\tau$ and to study its properties as well as the cross section of ν_τ and $\overline{\nu}_\tau$. The detector uses the technique of the Emulsion Cloud Chambers (ECC), which consist of a sequence of passive material plates interluded with emulsion films. [15]

4) Muon Magnetic Spectrometer The muon Magnetic Spectrometer, located downstream of the ECC, is part of the ν_τ detector. It consist of a dipole magnet, straw tubes and Resistive Plate Chambers (RPC). Its task is to identify the muons, produced in the neutrino interactions and τ decays, with high efficiency and to complement the muon momentum measurement performed in the ECC by extending the kinematic range. [15]

5) Hidden Sector Decay Volume The purpose of the Hidden Sector Detector is to search for decay vertices of hidden particles in a single large decay volume. The vessel is under vacuum at a level of 10^{-6} bar, this is necessary to achieve the required level of background rejection.

The conical vacuum vessel has a rectangular cross section of 2.6 m to 5.4 m width and 5.1 m to 10.3 m height and a total length of 50 m.[16] To further control background events, the vessel is surrounded by a background tagger consisting of liquid scintillators. [17]

6) Spectrometer The Spectrometer is placed at the rear end of the Hidden decay Volume and consist of a large aperture dipole magnet and two tracking telescopes using straw trackers on each side of the magnet. The spectrometer is used to reconstruct the tracks of charged particles from the decay of hidden particles and at the same time reject background events. The spectrometer must also determine the track momentum and flight direction within the decay volume. The extrapolation of the tracks has to be precise and well matched with the segmentation of the timing detector to use the high accuracy of the associated track time to remove combinatorial background. [10]

7) Veto Timing Detector A Veto detector identifies and vetos random crossings in the Decay vessel. Further detail about this part are written down in section 1.3.2.

8) Calorimeter The SHiP calorimeters identify particles and measure their position and energy. This information is used to improve the event reconstruction and particle identification. An electromagnetic calorimeter (ECAL) is placed downstream of the timing detector and is followed of the hadronic calorimeter (HCAL). It has been proposed to use a shashlik design with scintillators in the ECAL with 140 alternating layers of 1 mm lead and 2 mm scintillator. Alternative designs are in discussion (see [18]). For the HCAL, also a shashik design was proposed. [10]

9) Muon Detector The muon system, in conjunction with the ECAL and HCAL, is primarily designed to identify the muons, coming from decays via neutrino, vector and scalar portals, with high efficiency. It also supports the effort to avoid the misidentification of pions as muons. The μ-detector consist of scintillating bars with wavelength-shifting fibres read out with Silicon Photomultipliers. [19]

1.3.2 The Veto Timing Detector

Main sources of remaining background are:

- Neutrinos interacting with surrounding material
- Muons that are backscattered from the experimental hall
- Cosmic muons

The neutrinos stem from interactions of the primary protons and survive the hadron absorber and the muon shield. They can interact inelastically with the decay vessel. These interaction can produce long living heavy neutral particles which, when decaying, can mimic the topology and modes of of hidden particles in the decay volume. This is the most difficult background to handle.

All muons from the interactions of the primary protons will eventually reach the walls of the experimental hall. Some will be reflected back and either enter the decay volume or generate particles through inelastic scattering with the walls. Cosmic muons generate background in the same way.

Random combinations of tracks of muons and other charged particles can enter the decay volume and fake decay-vertices which resemble signal events, as shown in figure 1.12. One efficient way to distinguish random crossings from actual physics is to require a coincidence in time for

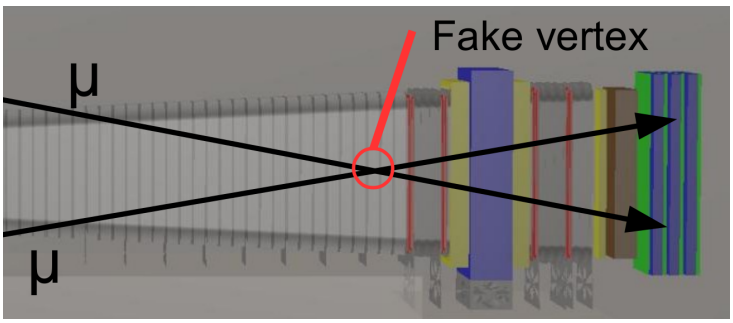

Figure 1.12: A random crossing of muon tracks from cosmic or backscattered muons create a fake vertex.

the tracks. In order to reduce the combinatorial di-muon background to an acceptable level, a timing resolution of 100 ps or smaller is required. Since the best time resolution that can be achieved by the other subdetectors of SHiP is in order of 1 ns, a dedicated timing detector is necessary. It will be placed in front of the ECAL.

For the timing detector, the following two options have been proposed:

- Plastic scintillating bars with Photo Multiplier Tubes (PMT) or Silicon Photo Multiplier (SiPM) readout
- Multigap Resistive Plate Chambers (MRPC)

A description of the option with MRPC can be found in the technical proposal of SHiP [10]. The option with the SiPMs and plastic scintillators is the main subject of these studies.

Arrays of plastic scintillating bars with lengths from 0.85 m to 4.5 m can efficiently cover large areas at relatively low cost. They also have the advantages of robust construction, low maintenance and reliability. Depending on bar length, scintillator type and light readout scheme, recent experiments have shown that such detectors achieve time resolutions in the range of 0.05 ns to 1 ns [20].

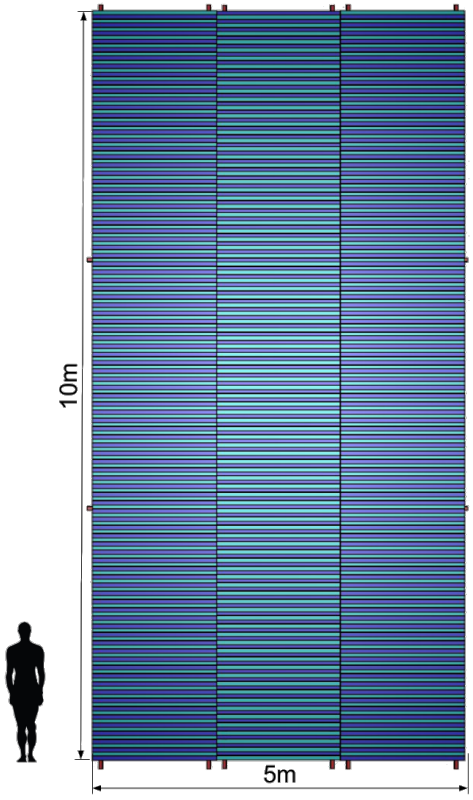

Figure 1.11: Current proposal for the design of the timing detector.

The geometry of the detector has changed over time. At present, the array consist of three columns of horizontal bars 168 cm long, 6 cm wide and 1 cm thick. To avoid inactive areas, the bars are staggered with an overlap of 0.5 cm vertically and 1 cm horizontally. In figure 1.11, there is a schematic of the current design. This design would need 546 bars in total, which would give a total of 1092 channels and a total of 8736 SiPMs[2]. [10]

[2]assuming 8 SiPMs per Channel, see section 4.2.1.

2 Devices and experimental setup

2.1 Silicon PhotoMultiplier (SiPM)

Silicon PhotoMultipliers (SiPM) are radiation detectors with high sensitivity to photons. They consist of array of Avalanche Photo Diodes (APDs) which are operated in Geiger mode. SiPMs detect with good efficiency and resolution light with a wavelength from about 400 nm to about 1000 nm. They are employed in environments with low light levels where a high precision measurement is required [21]. Some devices that use the same basic principles are Micro-Pixel Avalanche Photodiodes (MAPDs), Multi Photon Pixel Detectors (MPPDs), Digital Pixel Phodiodes (DPPDs) and Metal Resistive layer Semiconductors (MRS-APDs).

2.1.1 Working principle of a silicon detector

A silicon detector is made out of a monocrystalline silicon with [22]:

- Band gap energy of $\Delta E = 1.12\,\text{eV}$ (pure silicon at 300 K)
- Average energy to produce electron-hole (e-h) pair: 3.6 eV
- Most probable energy loss for a minimum ionizing particle: 2.75 MeV/cm

A minimal ionizing particle produces therefore around 23000 e-h pairs in a 300 µm thick silicon detector.

The following important concepts of a silicon detector are described bellow:

Silicon doping, n-type Group-V elements (Arsenic or Phosphorus) get included into the lattice of the silicon crystal as donor-atoms. The weakly bound excess electrons create a energy levels slightly bellow the conduction band increasing the Fermi Energy. See figure 2.1.

Silicon doping, p-type Group-III elements (Boron) get included into the lattice of the silicon crystal as acceptor-atoms. The weakly bound excess holes create a energy levels slightly above the valence band, lowering the Fermi Energy. See figure 2.2

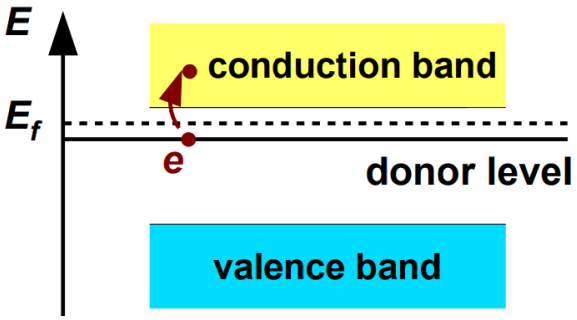

Figure 2.1: Fermi energy E_f in silicon with n-type doping. [22]

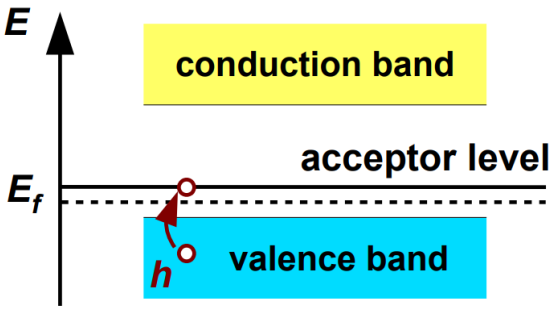

Figure 2.2: Fermi energy E_f in silicon with p-type doping. [22]

p-n junction n-doped and p-doped silicon meet at the p-n junction. The difference in the charge-carrier density leads to a diffusion across the junction. When the equilibrium between coulomb-force and diffusion is reached, the movement stops, which results in a depleted zone with very few charge carriers. Due to recombination of electrons and acceptor atoms on the p-side and recombination of holes and donor atoms on the n-side, an electric field arises as shown in figure 2.3.

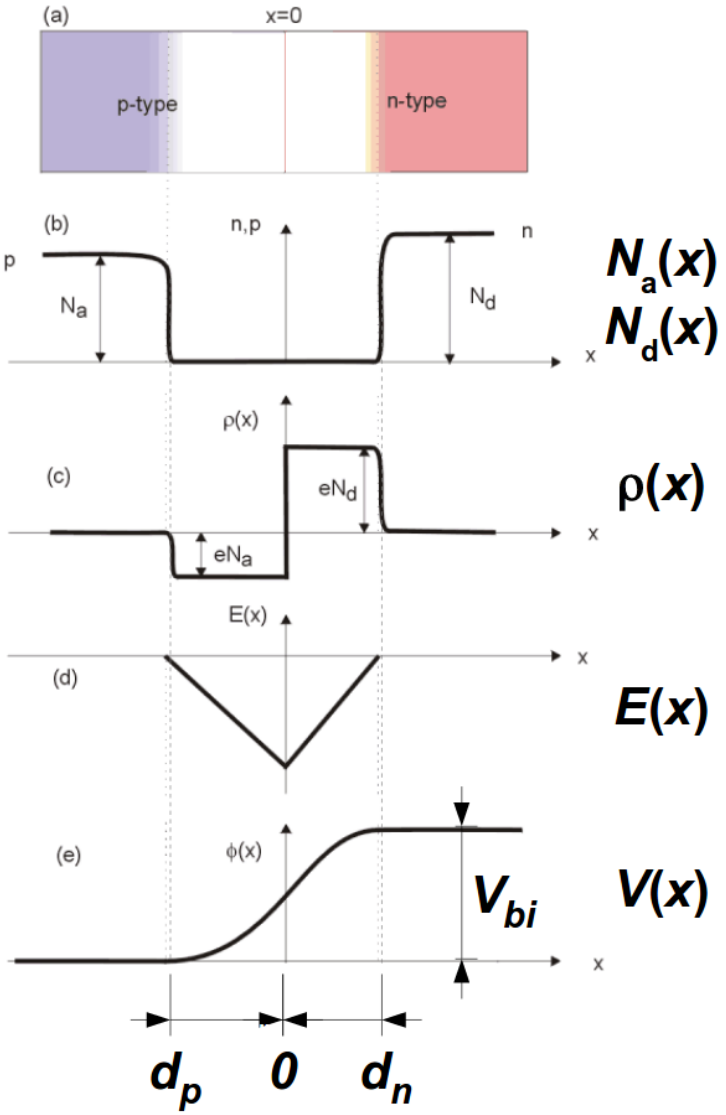

Figure 2.3: (a) p-n junction in equilibrium, (b) number of holes $N_a(x)$ and free electrones $N_d(x)$, (c) uneven charge density $\rho(x)$, (d) electric field $E(x)$ in x-direction, (e) the potential $V(x)$. The depletion zone goes from d_p to d_n. [22]

Reverse bias An external voltage with positive polarity at the n-side is applied to increase the width of the depletion zone. The free charge carriers are swept out of the depletion zone and the electric potential increases. If the depletion zone is as wide as the detector, the detector counts as "fully depleted". The Voltage for full depletion is found by measuring the capacitance of the device. The capacitance stays constant above the voltage for full depletion and there's a very small leakage current that resumes almost constant up to the Breakdown Voltage (BdV).

Forward bias To narrow the width of the depletion zone a negative voltage is applied to the n-side. If the depletion zone vanishes, i.e. the applied voltage is larger than the built-in voltage of the junction, then the junction becomes conductive.

2.1.2 Avalanche Photo Diode (APD)

An Avalanche Photo Diode (APD) is a silicon detector which is the semiconductor analog of the Photo Multiplier Tube (PMT). The schematics of an APD with four differently doped silicon zones are shown in figure 2.4. The small p^+ and n^+ region toward the anode on the front have the effect that the electric field gets peaked in this region. The p^- epitaxial region is fully depleted

due to the reversed bias applied on the back contact. This zone is also called absorption region, because the probability that an incoming photon gets absorbed is the highest. The electric field there is too low to cause impact ionization, therefore, no new e-h pairs get created, until the electron reaches the p^+ zone. The electric field in that zone is strong enough for the charge carrier to get the kinetic energy required to create additional e-h pairs via impact ionization. The newly created free charge carrier get enough energy to create another e-h pairs, leading to an avalanche of charge carriers. The APD in figure 2.4 has no avalanche layers on the side of the cathode and, since electrons move faster than holes, this sensor type recovers faster.

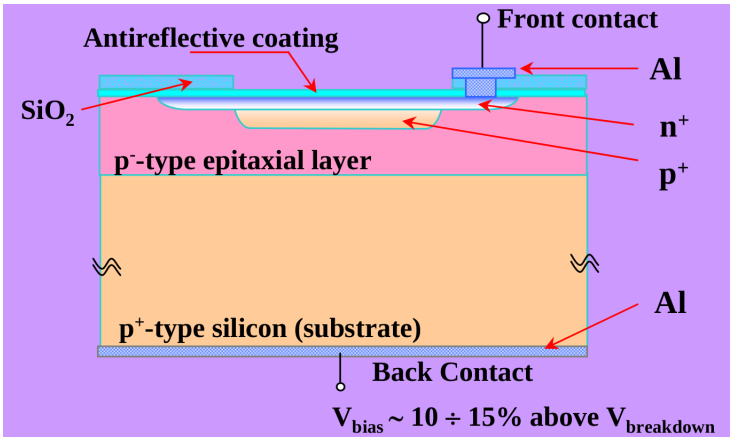

Figure 2.4: The APD schematic shows the cross section of an APD composed of four different regions of doped silicon. A photon gets absorbed in the epitaxial layer (absorption zone) and generates a a few e-h pairs. The electrons move up towards the front, the holes down to the back. In the p^+ and n^+ layers near the front, there is a peak in the electric field, which accelerates the electrons more. The accelerated electrons can produce new e-h pair,which also can produce e-h pairs. This multiplication process leads to concentrated avalanches in that region. [23]

Classically, APDs operate in proportional mode, with a reversed bias slightly below the BdV, so only electrons are involved in the avalanche process [24]. Despite the high detection efficiency, the gain of APDs is strongly dependant on the temperature and bias voltage, making it impossible to separate single photons from noise.

To improve the gain and stability, small area APDs are operated in the so called Geiger mode, in analogy to the Geiger counter. An APD cell in a SiPM is design to operate at a reverse bias voltage 5 % to 10 % above the BdV, the electric field being strong enough that a single photo-electron can cause an avalanche.

Due to impact ionization, electrons and holes constantly produce new e-h pairs, and this avalanche has to be quenched quickly before the APD can detect a new incoming photon. To quench the avalanches, a resistor is inserted in series with the APD as shown in figure 2.5. The creation of avalanches stops quickly due to a drop in voltage caused by the output current flowing through the quenching resistor. In this so called binary mode, any information about the primary signal gets lost due to the instantaneous reset to the initial state. [24]

Since thermally generated e-h pairs also cause avalanches in APDs, these diodes are limited in area. The dimension of an APD in a SiPM varies from 10 µm to 20 µm, therefore their density can reach 1000 per mm^2.

2.1.3 Working principle of a SiPM

A SiPM consist of a matrix of APDs as shown in figure 2.6. The APDs are in parallel as shown in figure 2.5, and are typically operated between 20 V to 100 V, about 15 to 75 times lower compared to the voltage required to operate a traditional PMT. Reading the APDs in parallel generates a signal amplitude proportional to the numbers of fired APDs. This makes it possible

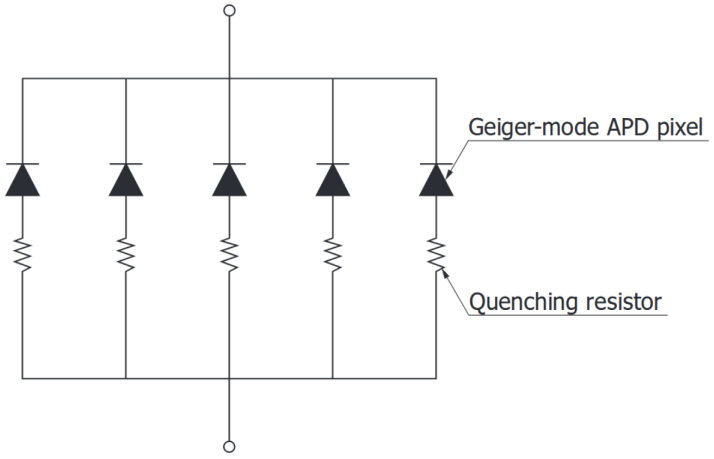

Figure 2.5: Schematic structure of an SiPM. The pixels are Geiger mode APDs and a quenching resistor in series. The SiPM consist of large number of these elements connected in series. [21]

to count the number of photons, assuming every fired APD was triggered by one photon. For this reason SiPMs are often referred as photon counters.

The main disadvantage of the SiPM over PMTs is the Dark Count in the SiPMs caused by thermally generated avalanches, depending on the operating voltage and the temperature of the SiPM. Dark count can be avoided by a dedicated trigger or by setting the trigger threshold above the single photon peak. The benefits of SiPMs over PMTs are [21]:

- SiPMs detect single photons with high efficiency
- SiPMs are not affected by magnetic fields
- SiPMs are resistant to mechanical shock
- SiPMs are less prone to light over saturation
- SiPMs are easy to operate
- SiPMs are more compact than PMTs

2.1.4 Characterization of SiPM

The following are the most important terms to characterize SiPMs and a short description of them.

Breakdown Voltage (BdV) The BdV is the minimal reverse voltage to make it conductive. The BdV is dependant of the temperature and it is important to know its value to be able to use the devices without damaging it. The BdV can widely change between different types of SiPM due to different doping and different thickness of the APDs.

Over Voltage (OV) The OV is given by:

$$\mathrm{OV} = V_{bias} - \mathrm{BdV} \tag{2.1}$$

where V_{bias} is the reverse bias voltage applied to the SiPM.

Nominal operating voltage The nominal operating voltage is usually about 10 % above the BdV of the SiPM, and at this voltage the SiPM has the best combination of efficiency, noise, photon resolution and timing resolution. The nominal operating voltage is usually given by the producer of the SiPM.

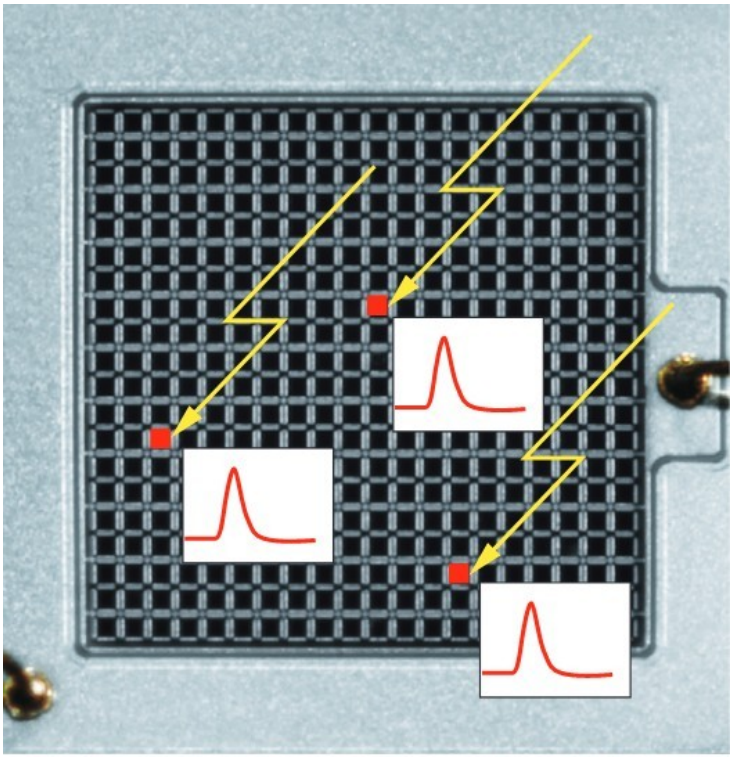

Figure 2.6: A close up image of the APDs in a matrix. [21]

Photon Detection Efficiency (PDE) The PDE describes the probability of detecting a single incoming photon. This is determined by:

- Quantum efficiency $Q_e(\lambda)$ [3]: The probability of an e-h pair being created by an incoming photon dependant on its wavelength
- Fill factor F: The ratio of the area of the detection window and total surface of the SiPM
- Triggering probability $T_e(V)$: The probability of a e-h pair to set off an avalanche

$$\mathrm{PDE}(\lambda, V) = Q_e(\lambda) \cdot F \cdot T_e(V) \tag{2.2}$$

Gain The gain G determines the charge produced in one avalanche and, in good approximation, is given by the pixel capacitance C_{pix}, the applied OV and the elementary charge q:

$$G \approx \frac{C_{pix} \cdot OV}{q} \tag{2.3}$$

Recovery time The recovery time is the time after an avalanche until a cell is fully sensitive again and it specifies the dead time of a pixel. During an avalanche in a pixel, V_{bias} drops down to the BdV, then recovers to the nominal operating voltage within an characteristic recovery time τ_r:

$$V_{bias}(t) = V_{bias}(0)\left(1 - e^{-\frac{t}{\tau_r}}\right) \tag{2.4}$$

The reduced bias voltage lowers the amount of charge which is produced by following avalanches. The recovery time can be determined by the capacitance of the APD, C_{pix}, and the quenching resistor R_q:

$$\tau_r = C_{pix} \cdot R_q \tag{2.5}$$

[3] The definition differs from the quantum efficiency for a PMT due to the cell structure of the device.

Cross Talk (CT) Charge carriers crossing a p-n junction can recombine, creating near infrared photons. These photons can travel into adjacent pixels and and initiate secondary avalanches as shown in figure 2.7. This effect is called CT and worsens the photon counting resolution due to the fluctuation in the number of fired pixels. The Cross Talk Probability (CTP) is strongly dependant on the OV and is defined by the numbers of simultanious firing pixels N:

$$CPT = \frac{N(\geq 2)}{N(\geq 1)} \tag{2.6}$$

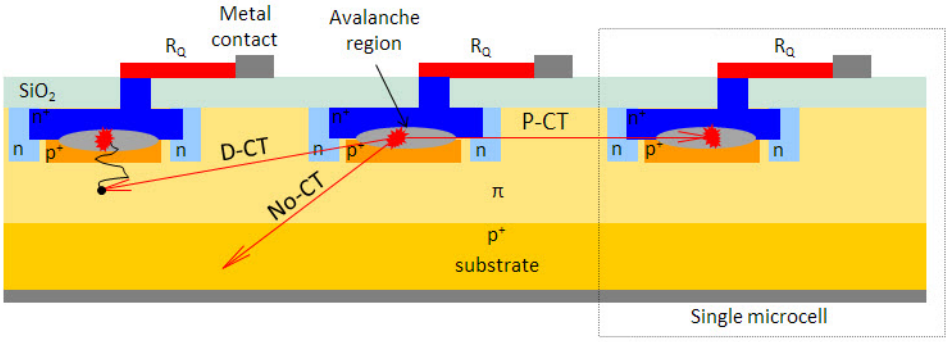

Figure 2.7: The three different cases for photons created in an avalanche: Simultaneous avalanche in an adjacent cell (P-CT), Photon creating e-h pair in the vicinity of neighboring cell triggering a delayed avalanche (D-CP) and a photon leaving the SiPM triggering no secondary avalanches (no-CT). [25].

Dark Count Rate (DCR) The DCR is the rate of occurring avalanches that were triggered without any incoming photons and includes mainly two components [26]:

- Thermal pulses: Avalanches triggered by thermal or field mediated excitations of electrons in the silicon lattice.
- After pulses: The silicon lattice or damages in that lattice can catch charge carriers and releases them up to microseconds later. This can also affect the recovery time.

Noise Pedestal noise[4] and gain fluctuation affect both the photon counting resolution and the time resolution. The noise is defined by the fluctuation of the baseline signal caused by leakage current and the readout electronics. Because the signal of the SiPM has to be amplified, the quality of the amplifier used is significant and it should introduce as little additional noise as possible.

Time resolution The time resolution is defined as the standard deviation σ_m of the measured time difference at a threshold V_{th} of the signal and a specified time t_0. The V_{th} don't has to be constant. The time resolution consist of several terms. Time walk σ_{TW} and electronic noise σ_{el} are the most significant ones. The other term are shortened to σ_{other} in this thesis. How the time is measured and how the time resolution is improved by offline analysis is described in section 3.

2.2 The MUSIC Board

The SiPMs are read out using a custom built ASIC called MUSIC (Multiple Use SiPM Integrated Circuit) provided by the University Barcelona [27]. It provides 8 individual analog single ended outputs and two summation channels in differential mode. For the single channel readout a extra

[4] referred as noise later on.

SMA-board has to be connected to the front side (see figure 2.8). Furthermore, it also provides a digital output, but this was never used in this study due to it's significantly worse timing resolution. On the front side of the board, there are connectors for up to 8 SiPMs for multiple different types of SiPMs from different manufacturers. On top of that, there is a connector on the backside of the board for an external array of SiPM with 8 channels. Another big advantage of the MUSIC board is, it does amplify the channels separately and sums them up afterwards. That decouples the intrinsic resistance and capacity of the SiPMs, which otherwise would increase the timing resolution [28].

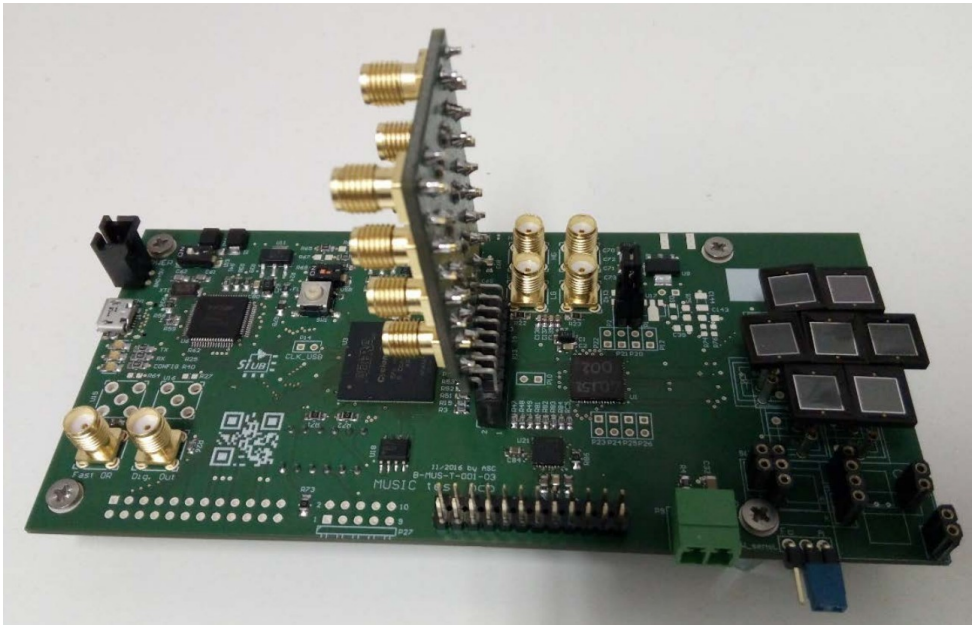

Figure 2.8: The frontside of the MUSIC-board with SMA board for individual readout and 7 Hamamatsu *HPK-S13360-6050CS* connected on right. [28]

If the MUSIC-board is connected via USB to a computer, the following can be controlled[29]:

- Choose between analog or digital output
- Control the voltage threshold of the digital output for each channel individually
- Start an automatic threshold-search for the digital output
- Start a digital photon count
- Control which SiPM is included in the sum
- Control a anode voltage offset for every SiPM individually for calibration
- The configuration of the board can be saved
- A saved configuration can be loaded onto the board
- Control Pole Zero (PZ) cancellation

The PZ sets two resistors, R_1 and R_2, and a capacitance C_1 on the input of the SiPMs, see figure 2.9, to shape the signal pulse. It takes two numbers: `R` to control both resistors and `C` for the capacitance. `R` is between 0 and 7 and `C` is between 0 and 31. The resistances of R_1 and R_2 that correspond to the number `R` are written down in table 2.1. The capacitance follows a linear distribution starting at 1.2 pF with steps of 0.1 pF.

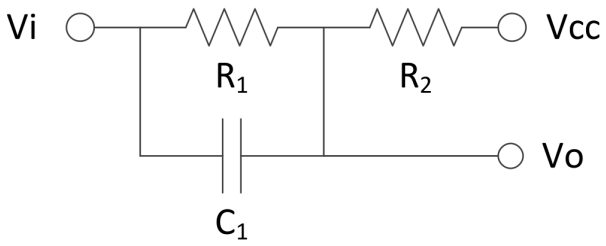

Figure 2.9: The pole zero shaper of th MUSIC board. R_1 and R_2 are controlled together, C_1 is controlled on its own. Vi is the input voltage coming from the input stage, which converts the input current of the SiPM into a voltage, Vcc is the power supply and Vo is the output voltage of the PZ circuit. [30]

R	R_1 [kΩ]	R_2 [kΩ]
0	18.60	7.65
1	20.40	5.85
2	22.20	4.05
3	24.00	2.25
4	24.45	1.80
5	24.90	1.35
6	25.35	0.90
7	25.80	0.45

Table 2.1: The values of the resistors R_1 and R_2 corresponding to the PZ setting number R. [30]

The PZ must be tuned in order to:

- Compensate under/overshoot of the signal.
- Reducing pulse width.
- Preserve the signal peak in light of excessive attenuation.

Figure 2.10 illustrates a typical signal before and after PZ cancellation.

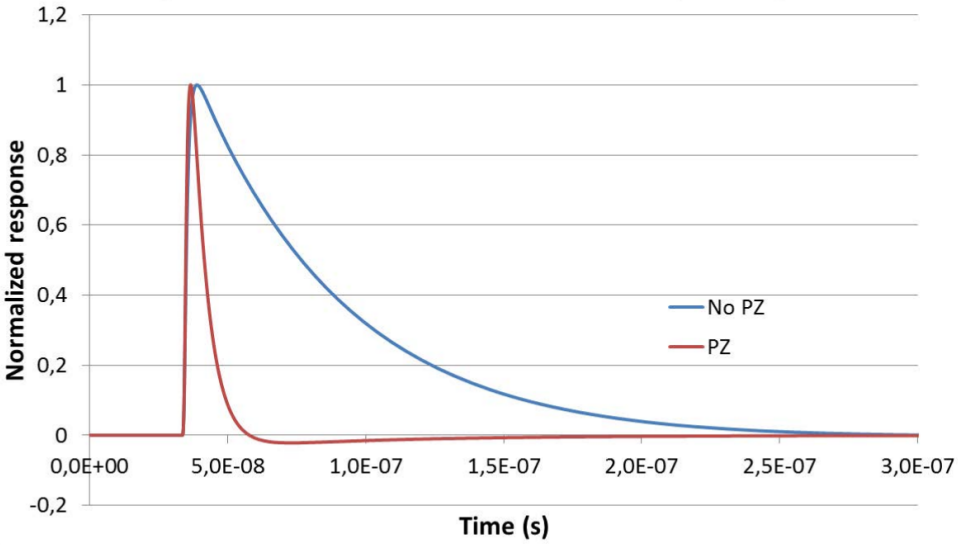

Figure 2.10: Comparison of a signal with pole zero cancellation and without. [30]

In our case, the PZ was set in a way that the MUSIC board has the best time resolution, i.e. lowest rise time. All the test were done with R3 C31 ($R_1 = 25.35\,\text{k}\Omega$, $R_2 = 0.90\,\text{k}\Omega$ and $C_1 = 3.3\,\text{pF}$) if nothing else is mentioned. The only disadvantage of those settings were that the

single photon resolution was lost (see section 3.8), because the one-photon amplitude is smaller than the noise. This was observed for all the settings.

2.3 Experimental setup

2.3.1 SiPMs and scintillating bars used

Different types of SiPMs were characterized in [31], and it was concluded that the best option are the SiPMs of the *HPK-S13360* series of Hamamatsu due to lower dark count rate, cross talk probability and single photon time resolution. In this thesis, arrays with 8 of Hamamatsus *HPK-S13360-6050PE* (see section A.1 in the appendix for characterization) in parallel mounted on MUSIC-boards (see section 2.2) were used for all the tests. All the SiPMs in one array are chosen in a way so their BdV is as close together as possible, so all of them can be operated at the optimal voltage. An array is shown in figure 2.11. The 8 SiPMs on the array cover only 10.5 % of the bar used in [31] and is therefore not sufficient to reach the goal of 100 ps time resolution on a scintillating bar with dimension 120 cm × 11 cm × 2.5 cm with a ^{90}Sr source, because it covers not enough area (see source [31]).

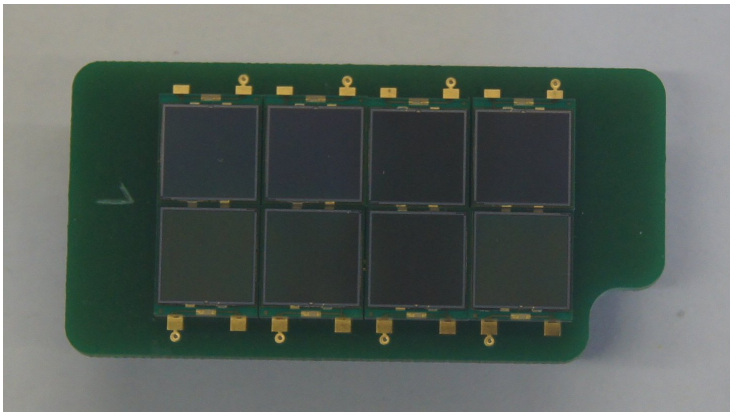

Figure 2.11: One of the arrays with 8 *HPK-S13360-6050PE* used in this thesis.

Two different types of organic scintillators were used, EJ200 and EJ230. Their differences can be read out in table 2.2 and all scintillating bar used in the test are listed in the table 2.3.

Property	EJ200 [32]	EJ230 [33]
Scintillation efficiency $[\frac{\text{photons}}{1\text{ MeV }e^-}]$	10 000	9700
Wavelenght of maximum emmision [nm]	425	391
Rise time [ns]	0.9	0.5
Decay time [ns]	2.1	1.5
Pulse with, FWHM [ns]	2.5	1.3

Table 2.2: The two different types of plastic in comparison.

plastic type	dimension	light guide	bar ID
EJ230	120 cm × 11 cm × 2.5 cm	no	1
EJ200	120 cm × 11 cm × 2.5 cm	no	2
EJ200	150 cm × 6 cm × 1 cm	no	3
EJ200	150 cm × 6 cm × 1 cm	yes	4

Table 2.3: List of scintillators used in the tests.

2.3.2 Setup in the lab

All the measurements in the lab were conducted in a custom made light tight box with the dimensions $1.8\,\mathrm{m} \times 0.7\,\mathrm{m} \times 0.4\,\mathrm{m}$ (see figure 2.12). The box was additionally covered with a rubberized black sheet, and the connection on the side of the box allow for the necessary connections to the electronics on the inside. The box is constructed with adjustable rails to hold the scintillator bars and a ^{90}Sr source which was pointed toward the scintillating bar. The source can be moved alongside the bar on the rail. A PCB with a SiPM of type *HPK-S13360-6050PE* by Hamamatsu, held on a stand between the source and the bar (see figure 2.15), was used as a trigger and it had a time resolution of $(244 \pm 5)\,\mathrm{ps}$, measured as described in section 3.5. It is the same box and railings used in [31] and the schematics of the setup are shown in figure 2.13. In section A.3 in the appendix are more details about the box and the railings. Bar 1 and bar 2 were tested in this setup.

Figure 2.12: The dark box used in the lab to shield the test setup from light.

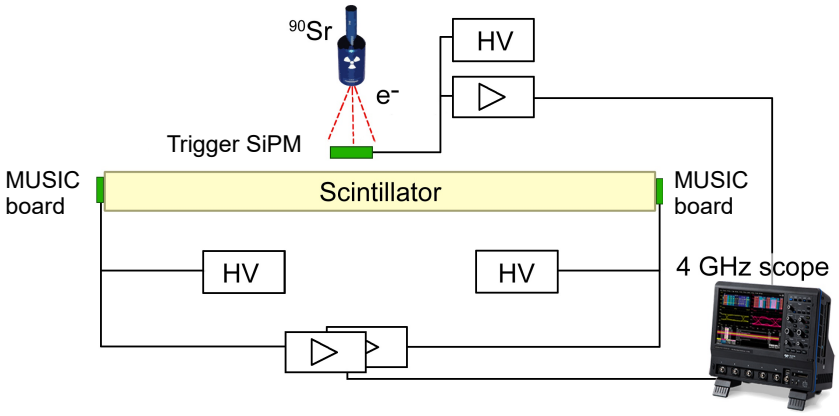

Figure 2.13: Setup of the tests in the lab. The source and trigger could be moved from side to side. [31]

The MUSIC-boards were held onto the ends by end-caps that were also used in the test beams (see figure 2.14 and 2.16). The trigger was held in between the source and the scintillator (see figure 2.15), so it was possible to perform a scan of the time resolution over the length of the bar. For all measurements the zero pole setting on the MUSIC-board was `R3 C31`. Measured were:

- Time resolution over the length the bar.
- Amplitude of the signal over the length of the bar.

The amplifiers of the trigger PCB and the MUSIC-board were biased by an *Aim TTi triple power supply* and the high voltage for the SiPMs was supplied by two *Kethley 237 High Voltage*

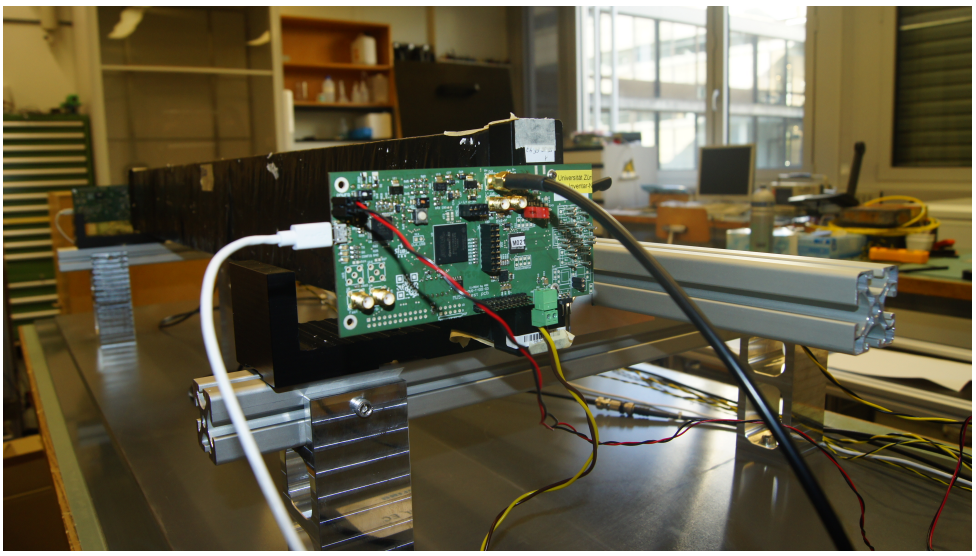

Figure 2.14: The MUSIC-boards were held onto the scintillator on adjustable railings. Not on the picture is the dark box, which was put over the experiment later on. Connected to the board are: USB for control (white), low voltage (red/black), high voltage (yellow/brown) and SMA signal cable (black).

Source-Measure Units. Both MUSIC-boards were connected in parallel to the low and high power supply, because they needed the same voltage for both voltages. To control the MUSIC-boards, two extra USB cables were connected to a Linux-computer outside the box. The trigger PCB on the other hand was connected individually to low and high voltage due to its different power consumption and it did not have a USB control cable.

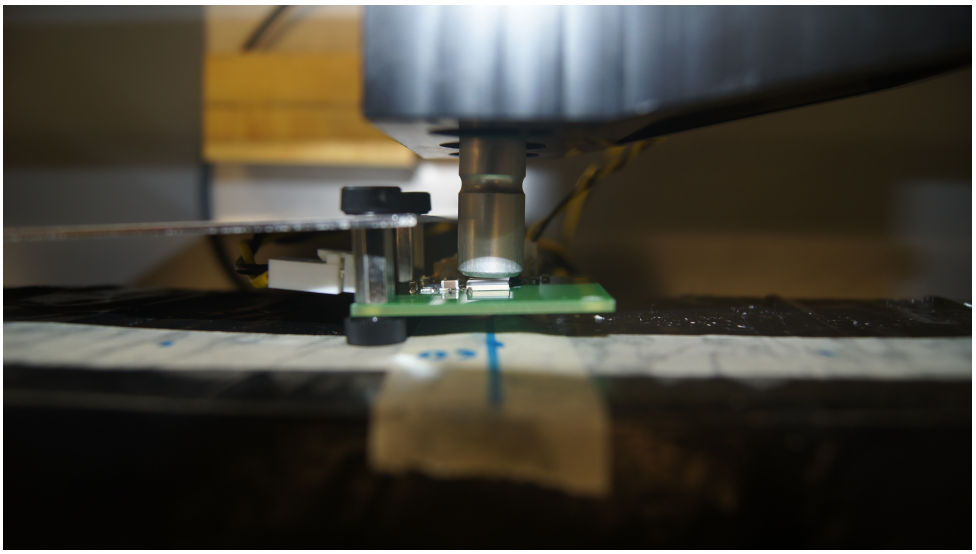

Figure 2.15: The trigger (green PCB) in the lab was set in between the ^{90}Sr source (metallic cylinder) and the scintillator.

To record the data, a *LeCroy Waverunner 8404M* 4 GHz oscilloscope was used. The Oscilloscope only has 4 channels available, therefore the differential output of the MUSIC board could not be used. It searched automatically for the constant fraction values (see section 3.1) of all three channels, calculated the time differences between the trigger and the signal of the MUSIC-boards, and put this two times into two histograms. After a measurement, the histograms got saved as a text file and loaded onto a computer where the offline analysis was done. The disadvantage of this method is that all the information except the time distribution gets lost. The advantage is that it is quick and simple.

2.3.3 Setup of the test beam

In June 2017 and October of the same year the scintillator bars were set up at the T9 test facility at CERN. The beam in June was a μ-beam with the energy of 1 GeV to 6 GeV. In October a mixed beam was provided with the same energies. For the tests at CERN, all the bars had to be wrapped into two layers of tin foil and electric tape to make them light tight. To make the ends of the bar lightproof, the SiPMs and MUSIC-boards were held on to the end-caps shown in figure 2.16.

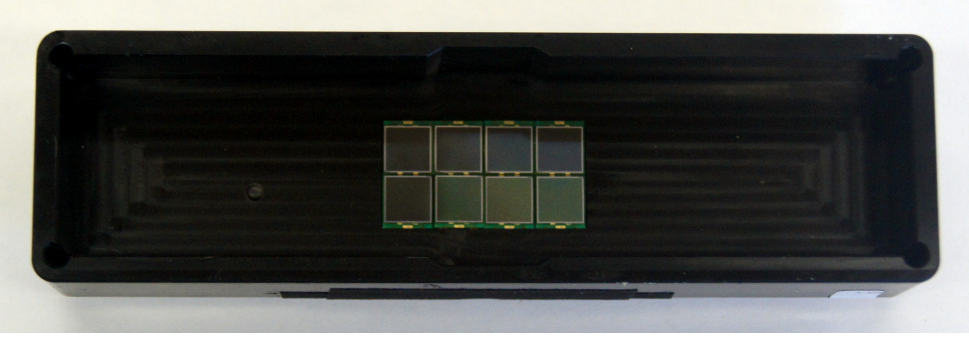

Figure 2.16: The end-cap of the bar that holds the SiPM in place and makes the bar lightight for the test at CERN.

As trigger, two small scintillator of the type EJ228 with the size of 2 cm × 2 cm × 2 cm were used. The readout of those were done with two PMTs on each scintillator and the time resolution of the trigger was (19.7 ± 0.1) ps.

A veto-system was also implemented. It consisted of a scintillator with a hole of radius 0.75 cm in it and was read out by PMTs. It was set up so the particle beam would go through the hole. If the veto-scintillator registered a particle, then this event would be ignored in the analysis.

In both test beams, the same hardware for the power supply was used. All the MUSIC-boards were connected to the high and low voltage supply. The PMTs of the trigger system only needed a high voltage supply, which was given by the *NDT1470* by CAEN. The waveforms of all four trigger-PMTs, two veto-PMTS and all MUSIC-boards were recorded by the 16-channel waveform digitizer *WaveCatcher*[34] into binary files for the offline analysis. There were enough channels on the *WaveCatcher* to record the differential output of the MUSIC boards. One of the MUSIC-boards was damaged during the test and could not be use anymore.

Test beam in June In June, the time resolution of bar 1, bar 2 and bar 3 were measured in a muon-beam at CERN.

The schematics of the setup can be seen in figure 2.17 For all the measurements the pole zero setting on the MUSIC-board was `R3 C31`.

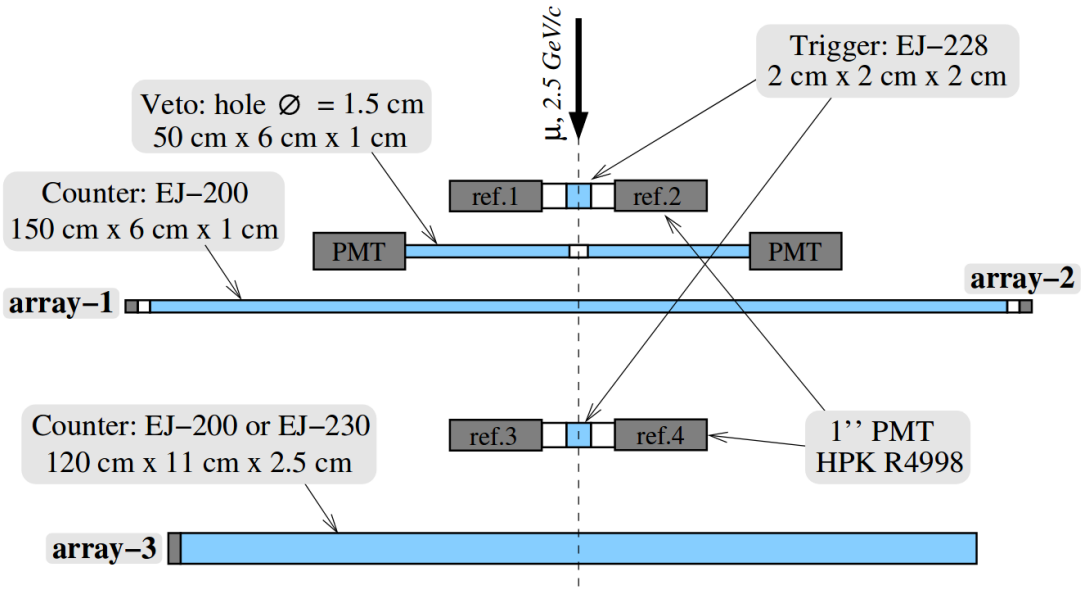

Figure 2.17: Setup of the tests in the beam in June 2017. [35]

the following scans were done:

- Voltage scan: The bias voltage was varied from 54 V to 63.5 V in half Volt steps for the bars of type EJ200 (see section 4.1).
- Constant fraction scan: the constant fraction value (see section 3.1) was varied between 0.01 and 0.5 in 0.01 steps, the result can be seen in section 3.1.1.
- Number of SiPM scan: turning the SiPMs on one after the other, on bar 2.
- Distance scan: The bars were moved horizontally, perpendicular to the beam.
- Signal amplitude versus time resolution.

The voltage scan was performed first, in order to figure out which voltage gave the best time resolution. The voltage with the best time resolution (58 V) was then applied in all the other tests. The result of the other test are shown in the sections 3.1.1, 4.2.1 and 4.2.3.

The results of this test beam were also used in [35].

Test beam in October During the test beam in October, bar 3 and bar 4, two settings on the MUSIC-board and two different SiPM arrays were tested. The test location was the same as at the test beam in June.

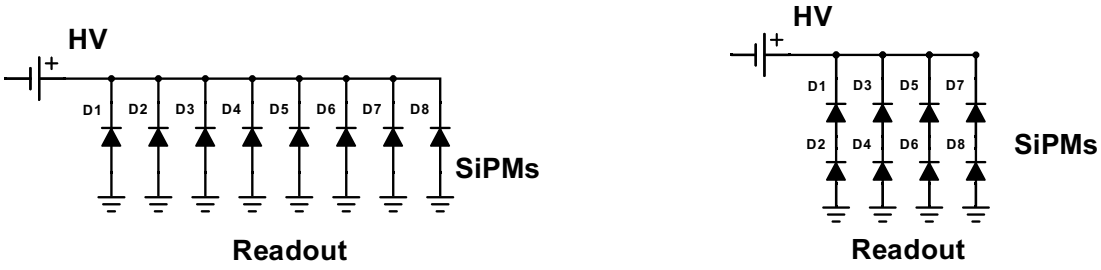

Figure 2.18: On the left is the normal array with 8 SiPMs in parallel, on the right the alternative with two SiPMs in series, four times parallel. The one on the left will be referred as 8×1 array and the one on the right as 4×2 array. If it is not specified, the 8×1 array was used.

The general setup was kept similar as in the test beam in June, with the exception of an additional counter 10 m upstream, consisting of a 4 cm × 4 cm × 0.5 cm scintillator of type EJ228 readout by two PMTs. This counter had a time resolution of (52 ± 1) ps and was necessary to do a Time of Flight (ToF) measurement. The power supply was identical to the test beam in June, so was the trigger near the tested bars. This trigger had the same time resolution as in the test beam in June ((19.7 ± 0.1) ps). The setup is shown in figure 2.19. The following tests were done:

- Different pole zero setting: One measurement was done with the pole zero setting `R3 C31` ($R_1 = 25.35\,\mathrm{k\Omega}$, $R_2 = 0.9\,\mathrm{k\Omega}$ and $C_1 = 3.3\,\mathrm{pF}$) and one with `R5 C12`($R_1 = 24.9\,\mathrm{k\Omega}$, $R_2 = 1.35\,\mathrm{k\Omega}$ and $C_1 = 2.6\,\mathrm{pF}$).
- Difference between the 4×2 and the 8×1 array.
- Difference of bars with light-guide and without.
- A Time of Flight (ToF) measurement between the bar and the first reference with the momentum of the particles ranging from 1 GeV to 6 GeV in steps of 1 GeV.

For all these tests except ToF measurement, a distance scan with a muon-beam was carried out. For the ToF measurement, the beam was switched to a mixed particle beam. The results can be seen in sections 4.2.5, 4.2.6, 4.2.7 and 4.3.

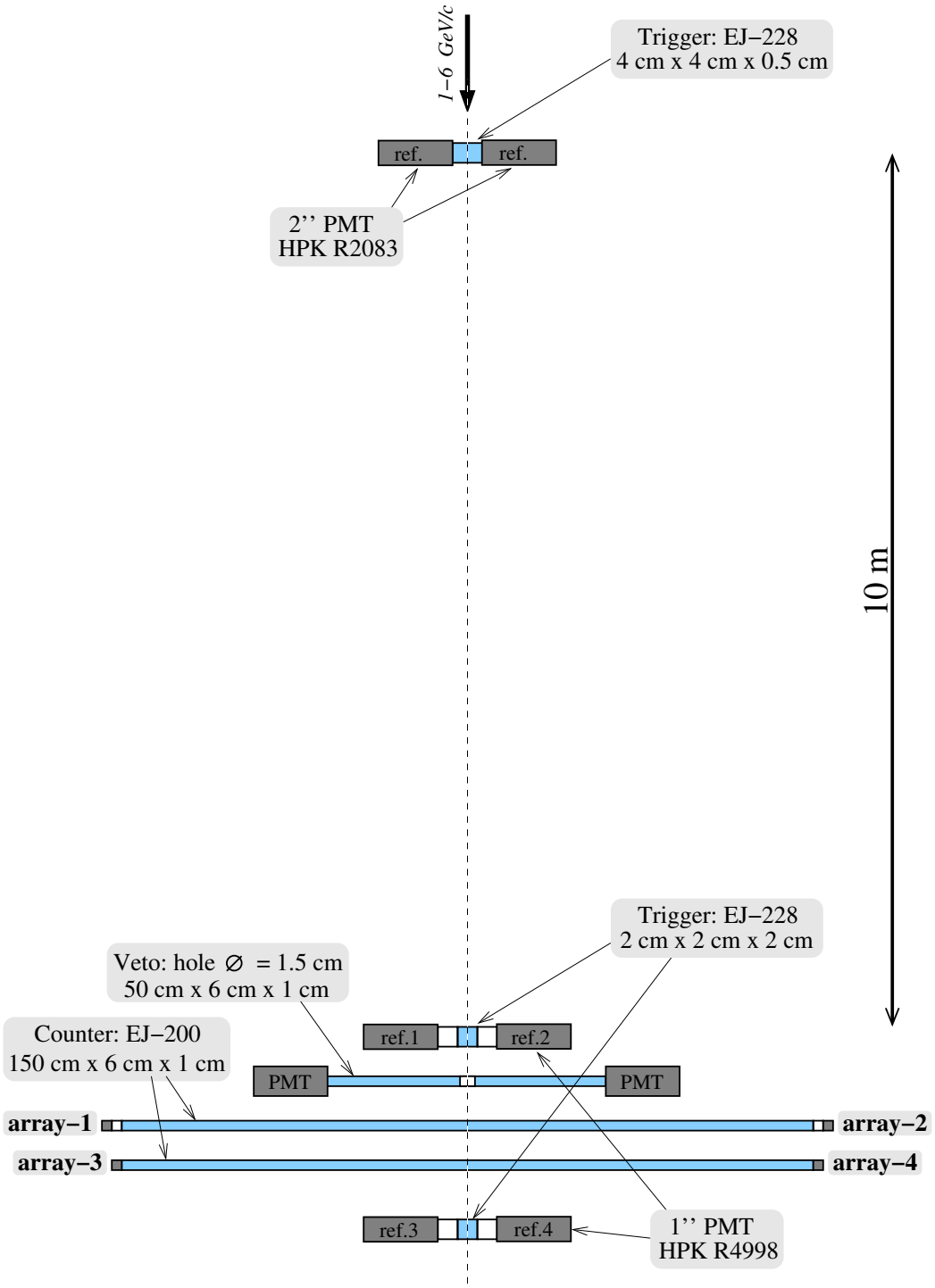

Figure 2.19: Setup of the tests in the beam in 2017 in October[5].

[5]The schematics were provided by Alexander Korzenev.

3 Methods of Software analysis

3.1 Constant fraction

In any analog measurement, the timing error due to time walk is unavoidable. Time walk is the effect that larger signals cross a certain constant threshold faster than smaller, given the rise time stays the same.

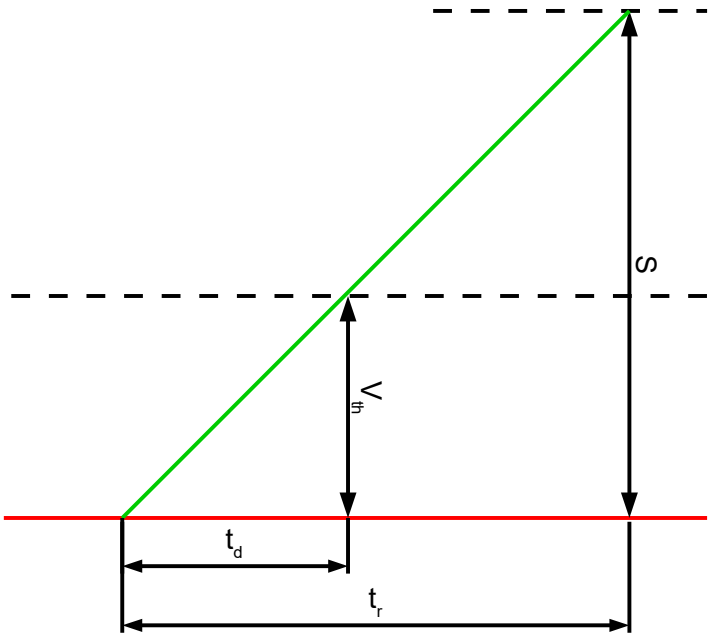

Figure 3.1: A simplified model of the relation between time delay t_d, rise time t_r, signal amplitude S and threshold V_{th}. [36]

From the simplified model of a signal in figure 3.1, it can be derived:

$$t_d = \frac{V_{th}}{S} t_r \tag{3.1}$$

with the time delay t_d, the threshold voltage V_{th}, the rise time t_r and the signal amplitude S. The timing uncertainty due to to time walk σ_{TW} is defined as the Root Mean Square of the time distribution:

$$\sigma_{TW} = [t_d]_{RMS} = \left[\frac{V_{th}}{S} t_r\right]_{RMS} \tag{3.2}$$

If V_{th} gets replaced by a constant fraction CF of the signal, $V_{th} = S \cdot CF$, we get:

$$\sigma_{TW} = [t_r]_{RMS} \cdot CF \tag{3.3}$$

In equation 3.3 and as an example in figure 3.2, it is easy to see that the error due to time walk reduces drastically, if a constant fraction discriminator with a small fraction is used [36].

The constant fraction should not be to small due to the electronic noise that comes from the amplifiers, SiPMs and other electronic parts in the experiment, see figure 3.3. The time uncertainty due to electronic noise σ_{el} is inverse proportional to the slope of the signal $\frac{dV}{dt}$ at the threshold [36]:

$$(\sigma_{el})^2 = \left(\frac{V_{RMS}}{\frac{dV}{dt}}\right)^2 \tag{3.4}$$

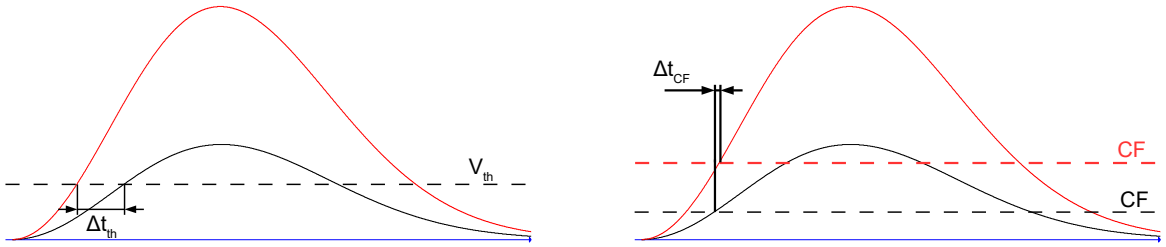

Figure 3.2: A simple example to show the time resolution improvement by choosing a CF discriminator (right) instead of a threshold-discriminator (left).

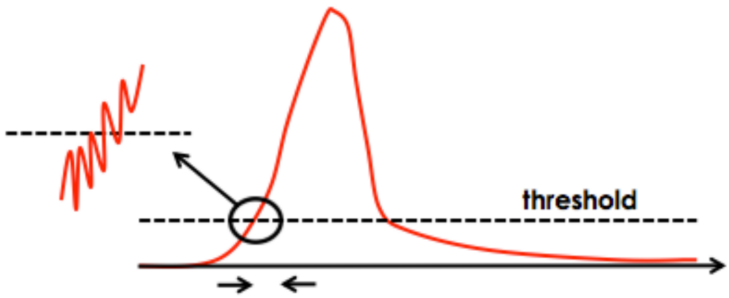

Figure 3.3: The electronic noise causes an uncertainty on the measured time. [36]

V_{RMS} is the Root Mean Square of the baseline voltage.

The V-t curve of the signal can be approximated with a Taylor approximation in the beginning of the signal (the moment, the photon arrives at the SiPM). The leading order of the expansion is quadratic:

$$V(t) \propto t^2 \tag{3.5}$$

$$\Rightarrow \frac{dV}{dt} \propto t \tag{3.6}$$

Where $t = 0$ the beginning of the signal is. If the $\frac{dV}{dt}$ in equation 3.4 gets substituted with equation 3.6, it follows that:

$$\sigma_{el} \propto \frac{1}{t} \tag{3.7}$$

$$\Rightarrow \sigma_{el} \propto \frac{1}{\sqrt{CF}} \tag{3.8}$$

This leads, for small constant fraction values, to a competitive effect between σ_{TW}, which decreases for decreasing constant fraction CF, and σ_{el}, which decreases with increasing CF. Thus it is important to scan CF in order to find an optimum value.

For larger CF, the slope of the signal, $\frac{dV}{dt}$, becomes constant, and σ_{el} gets constant.

The total error on the time measurement is:

$$\sigma_{tot} = \sqrt{\sigma_{el}^2 + \sigma_{TW}^2 + \sigma_{other}^2} \tag{3.9}$$

3.1.1 Constant fraction scan

In figure 3.4 the result of the CF-scan is shown. The data for the beam was obtained by one measurement in the middle of the bar and a CF-scan in the offline analysis (as described in section 3.3) with about 2000 events. The values of the lab were measured as follows:

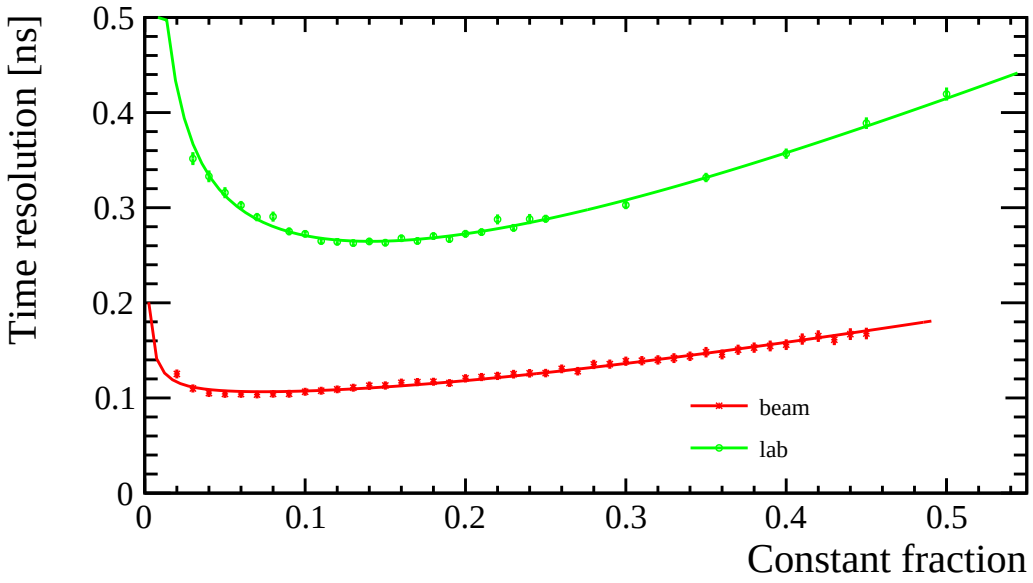

Figure 3.4: Constant fraction scan $CF = 0.05$ for the beam and $CF = 0.1$ for the lab has been chosen. The fit is equation 3.10. The data from the beam was not corrected and the trigger time-resolution was not subtracted and bar 3 was used. The data from the lab was taken without any trigger and bar 1 was used. Both measurement were done with 8 SiPMs.

1. Set CF-value
2. Start measurement as described in section 3.2
3. After enough events have been recorded (about 20 000 events), save the data
4. Begin at point 1 with new CF-value

Onto the graphs the parameters a, b and c of the following function were fitted.

$$f(CF) = \sqrt{a^2 + \frac{b^2}{CF} + (c \cdot CF)^2} \tag{3.10}$$

The function is derived from equation 3.9, with

- a: Constant error
- $\frac{b}{\sqrt{CF}}$: Error from electronic noise σ_{el}
- $c \cdot CF$: Error of the time walk σ_{TW}

	a	b	c
beam	(0.099 ± 0.001) ns	(0.0087 ± 0.0008) ns	(0.307 ± 0.005) ns
lab	(0.199 ± 0.002) ns	(0.053 ± 0.001) ns	(0.711 ± 0.008) ns

Table 3.1: The fit result of the CF-scan

The result of the fit can be seen in table 3.1. The difference between the measurement in the lab and the beam comes from the fact that the measurement in the beam has generally a better time resolution. Add to that, the measurement in the lab was done without trigger, and the measured time is the time difference between the MUSIC-board signals, but this should not affect the minimum CF-value, which is the value searched for in this test.

The difference in the optimum CF-value between the lab and the beam comes from the different signal strength due to more photons produced at the beam and the possibility to use the differential mode at CERN. The tests at CERN have shown a much higher signal amplitude,

and therefore the slope of the signal $\frac{dV}{dt}$ is larger even at the beginning of the signal, so a lower value for CF can be chosen.

In the end a CF-value of 5 % for the beam and 10 % for the lab was chosen.

3.2 Measurement in the lab

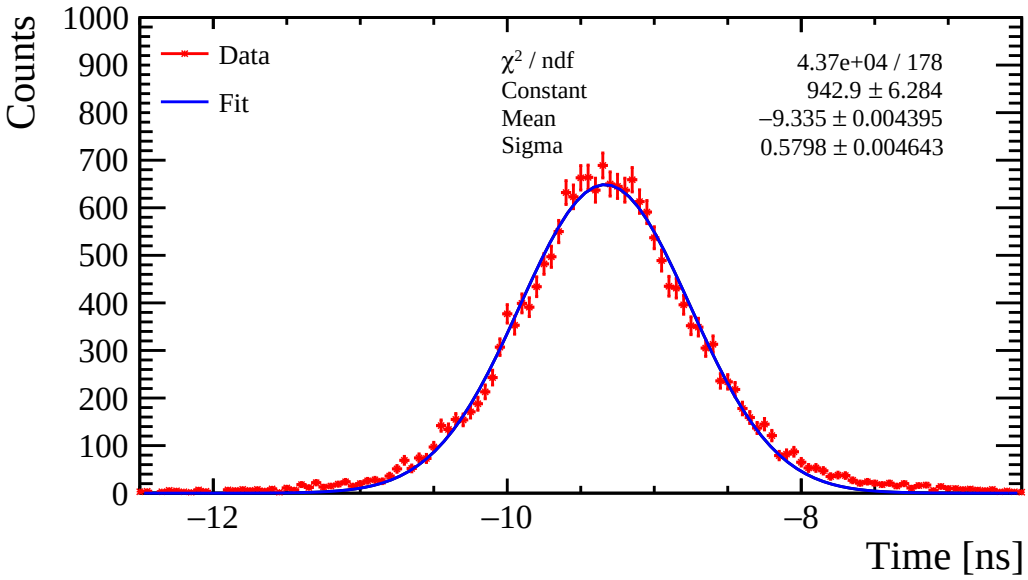

Figure 3.5: An example of a histogram collected by the Waverunner in the lab of the time differences of the trigger board and a MUSIC-board, done with bar 2 and bias voltage of 58 V, fitted with a Gaussian.

The Waverunner used in the lab finds the constant fraction automatically and calculates the time t_{CF} Furthermore, the scope was set up to calculate the measured time t_m as follows:

$$t_m = t_{CF} - \frac{1}{n}\sum_{i=1}^{n} t_{CF;trigger_i} \tag{3.11}$$

where n is the number of triggers, which was one in the laboratory. The scope collects the t_m in a histogram, which is saved for the offline analysis. The offline analysis consists of simple Gaussian fit of said histogram, as seen in figure 3.5.

The σ_m of the fit $A \cdot exp\left(\frac{(x-\mu)^2}{2\sigma_m^2}\right)$ is defined as the time resolution of that system, to get the real time resolution of the MUSIC-board, equation 3.13 has to be applied.

3.3 Measurement in CERN

At CERN, the Wavecatcher saved the waveform as pairs of $(t_i, V(t_i))$ of all the triggers and MUSIC-boards (see figure 3.6 for a signal of the MUSIC-board). Therefor the offline analysis did consist also of an algorithm to search for the maximum and the CF-crossing point. The algorithm follows the following steps for every recorded event:

1. Do the following for all the trigger-channels and the channel of the MUSIC-board:
   (a) Subtract the differential channels from each other (Only for the MUSIC board channels)
   (b) Find maximum of the peak V_{max}
   (c) Calculate the level of the constant fraction: $V_{CF} = V_{max} \cdot CF$

(d) Find first point, which is $V(t_i) > V_{CF}$ for $i = \{j, j+1, ..., j+n\}$, n something between 5 and 10

(e) Solve $V'(t_{CF}) = V_{CF}$ for t_{CF}, where $V'(t)$ is linear interpolation between $V(t_j)$ and $V(t_{j-1})$

2. Calculate t_m with equation 3.11
3. Start at point 1 for the next event
4. After all events are saved, calculate the time walk correction (see section 3.6)

The t_m get collected in a histogram, and then the σ_m is calculated the same way as in the measurement in the lab.

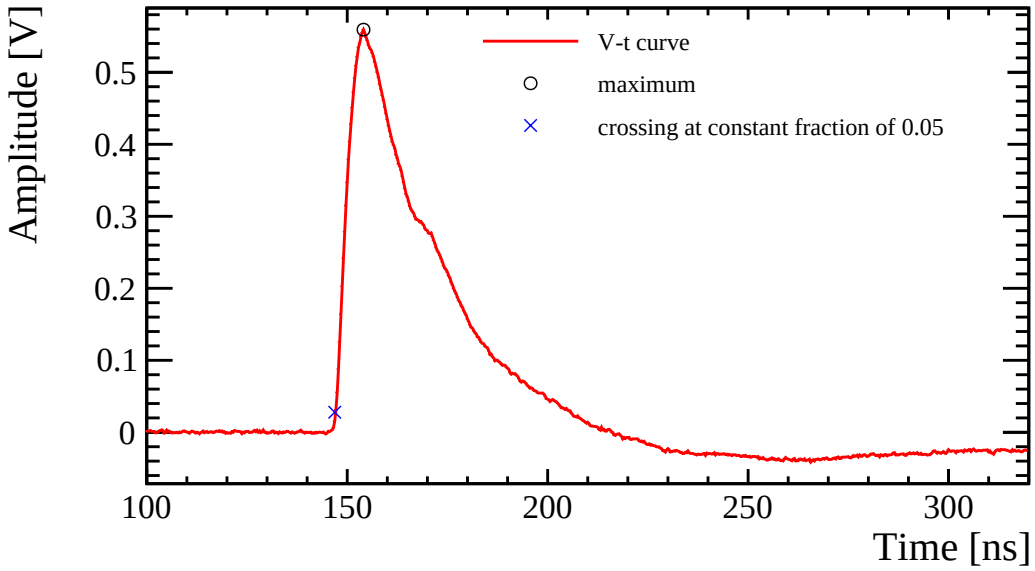

Figure 3.6: A Waveform of the SiPM array of the MUSIC board.

3.4 Calculation of the time resolution

The histogram of the measured time difference t_m were fitted with a Gaussian:

$$f(t) = A \cdot exp\left(\frac{(t-\mu)^2}{2\sigma_m^2}\right) \tag{3.12}$$

with the scaling A, the average time difference μ and the time resolution σ_m. The important value of this fit is the σ_m. The actual time resolution of the SiPMs at the scintillating bar gets calculated as follows:

$$\sigma = \sqrt{\sigma_m^2 - \sigma_{trigger}^2} \tag{3.13}$$

To evaluate the time resolution of the trigger $\sigma_{trigger}$, two different cases did occur, both are discussed below in section 3.5.

3.5 Trigger time resolution

Trigger time resolution with one trigger To calculate the time resolution of the scintillating bar, the timing resolution of the the trigger has to be evaluated first. In the case when there was only one trigger available, its time resolution could be calculated with the scintillating bar acting

as a trigger, by putting the source in the middle of the bar and assuming that read out of either end of the bar gives the same time resolution, which was evaluated as follows:

1. Get $t_m = t_{CF;1} - t_{CF;2}$, with $t_{CF;i}$ the CF-crossing time of the signal of the MUSIC-boards
2. Collect the t_m in a histogram, and fit a Gaussian for the $\sigma_{m;2\times MUSIC}$
3. Perform timing measurement with equation 3.11, where $t_{CF;trigger}$ are now the CF-crossing times of the MUSIC-boards
4. Fit a Gaussian of the distribution of that measurement
5. Calculate the timing resolution of the trigger with equation 3.13, with $\sigma_{trigger} = \frac{\sigma_{m;2\times MUSIC}}{2}$

Trigger time resolution with four triggers In the measurement done at CERN, there were always 4 triggers available. Assuming that all the triggers have the same time resolution, t_m could be evaluated as follows:

$$t_m = \frac{1}{2} \cdot (t_{CF;1} + t_{CF;2}) - \frac{1}{2} \cdot (t_{CF;3} + t_{CF;4}) \tag{3.14}$$

with $t_{CF;n}$ the CF-crossing times of the triggers 1 to 4. σ_m gets evaluated with a Gaussian fit as before, and the combined trigger time resolution is

$$\sigma_{trigger} = \frac{\sigma_m}{2} \tag{3.15}$$

3.6 Time walk correction

Because the DAQ during the testbeams at CERN saved the waveforms, the correlation between the signal amplitude and t_m could be used to improve the time resolution further. In the lab this correction was not applied since the individual waveforms were not saved. The algorithm of this so called time-walk correction works as follows:

1. Collect pairs (amplitude V_{max}, t_m), with A the maximum voltage of an event, of all events of one measurement and put them into amplitude/time diagram (see figure 3.7).
2. Fit $t(V) = a \cdot V^2 + b \cdot V + c$ onto that graph to get the correction parameters a, b and c.
3. Calculate $k = \frac{-1}{4} \cdot \frac{b^2}{2a} + c$.
4. Apply the correction $t_{m;corrected} = t_m + k - t(V_{max})$.

If nothing else is mentioned, then the correction were applied to the data of the tests with beams.

The effects of the correction can be seen in figure 3.7 (before correction) and figure 3.8 (after correction). The effect on time resolution can be seen in figure B.1. It improves the time resolution between 0% and 8%.

3.7 Time resolution of mean and weighted mean

The time resolution of the bar can be improved significantly by measuring the light on both sides of the scintillator ($t_{CF;1}$ and $t_{CF;2}$) at the same time and then taking the average of both (see equation 3.16), or, if the time resolution of both sides are know, taking the weighted average (see equation 3.17 [37]).

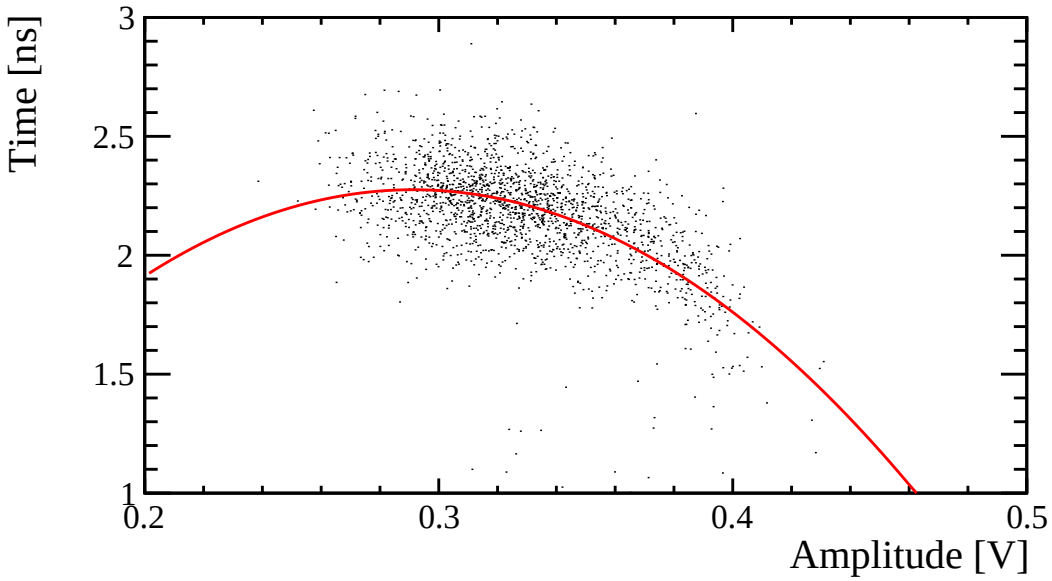

Figure 3.7: Scaterplot amplitude- time before correction.

$$\text{mean} \quad t_m = \frac{t_{CF;1} + t_{CF;2}}{2} \tag{3.16}$$

$$\text{weighted mean} \quad t_m = \frac{t_{CF;1}/\sigma_1^2 + t_{CF;2}/\sigma_2^2}{1/\sigma_1^2 + 1/\sigma_2^2} \tag{3.17}$$

The time walk correction has to be applied before the average or weighted average is taken. The t_m get collected in a histogram and the analysis is performed as before.

3.8 Amplitude analysis

An important part of this thesis was to verify the assumption that the time resolution depends on the detected number of photons as follows:

$$\sigma \propto N^{-0.5} \tag{3.18}$$

This could either be done by performing a time resolution measurement with a different number of SiPMs turned on assuming the photons are distributed evenly at the end of the bars, or the amplitude of the signal gets measured directly, and their distribution gets fitted with the Poisson distribution:

$$f(x) = A \cdot \left[e^{-\lambda} \cdot \frac{(\lambda)^{x/s}}{\Gamma((x/s)+1)} \right] \tag{3.19}$$

where A is a normfactor, λ is the average number of photons and s is the amplitude of the one-photon peak, which was held constant over all measurements of one distance scan, by measuring it with dark count and setting it to its value during the fit. In figure 4.3, there is an example of a fit with data from the lab and in figure 4.4, there is an example for a fit with the data from CERN. As seen in both examples, it is impossible to distinguish the different photon peaks due to the settings of the MUSIC-board and possible bad calibration and electronic noise, but it is still possible to fit for the number of photons. The result of this measurement can be seen in section 4.2.2.

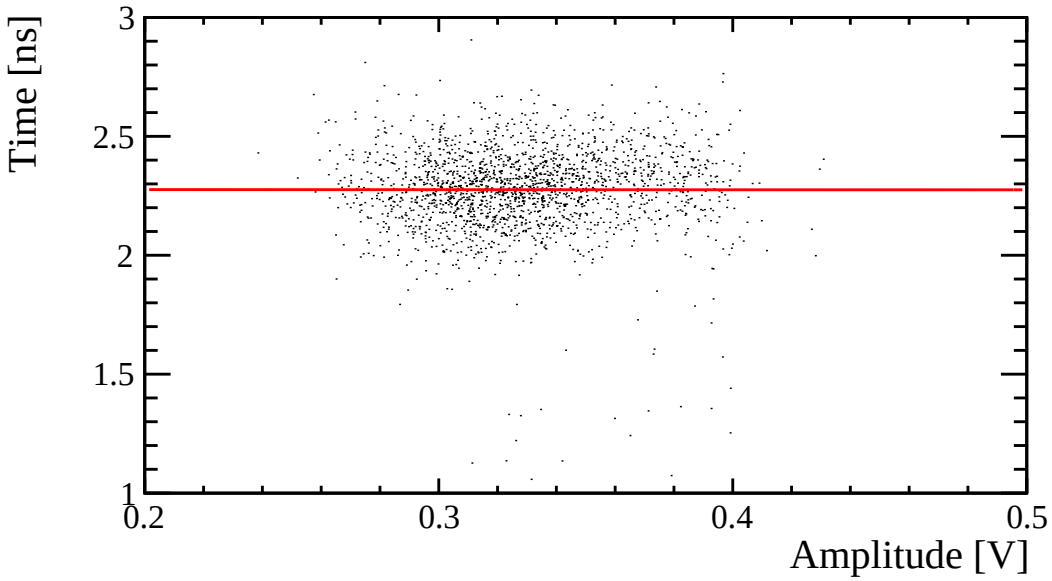

Figure 3.8: Scaterplot amplitude- time after correction.

3.9 Monte Carlo simulation

To test if the time resolution is better than the required 100 ps for a longer bar with the same profile as the tested, e.g. with dimension 170 cm × 6 cm × 1 cm, a simple Monte Carlo simulation was performed to extrapolate the results from a 150 cm long bar. The simulation followed the steps:

1. Get the time resolution of the single boards and fit the distance scan with a suitable equation for an extrapolation.
2. Assuming symmetric system mirror the fit for the other side ($f_{re}(x) = f(x_{max} - x)$).
3. For point x, generate events with Gaussian distribution with $\sigma = f(x)$ and $\sigma = f_{re}(x)$.
4. Calculate t_m according to equations 3.16 and 3.17 and collect them in a histogram.
5. From the distribution of t_m, calculate the timing resolution as before.
6. repeat step 3 to 5 for all different points on the bar for a distance scan.

It is important to mention that the result of this simulation is not verified and should be taken with a grain of salt due to the extrapolation, but due to the current design of the timing detector with bars of the length 168 cm (see section 1.3.2) it would be nice to know if the time resolution is sufficient.

4 Results

4.1 Voltage scan

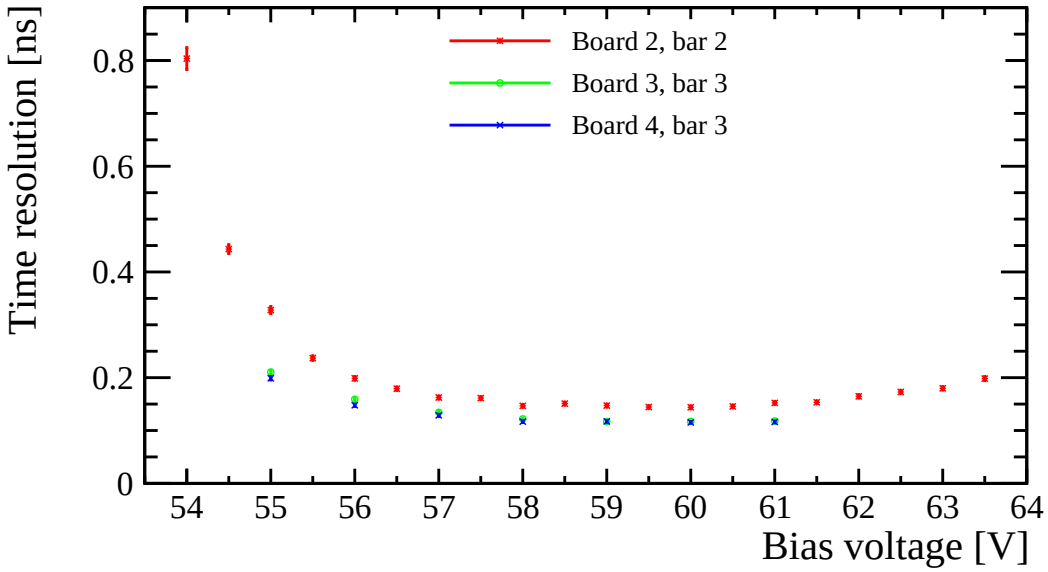

Figure 4.1: Voltage scan from the beam. Bars 2 and 3 were used.

The first measurement at the beam in June was the voltage scan. The beam was aimed at the center of the bar and the CF value was 5 %, only the bias voltage on the SiPMs was changed. The result of the measurement is shown in figure 4.1 for bars 2 and 3.

Surprisingly, the best time resolution is not at the proposed operating voltage by the manufacturer of ∼55 V, but higher. A possible reason for that is, that the manufacturer optimizes this voltage for one single SiPM detecting single photons, and in this measurement an array of 8 SiPMs have been used to detect up to 60 photons. After this test it was decided that all the test were done with a bias voltage V_{bias} of 58 V.

4.2 Timing resolution measurements

4.2.1 The time resolution versus of the number of SiPMs

The time resolution versus of the number of SiPMs was measured by:

1. Read out only a certain number of SiPMs
2. Measure the time resolution as described in section 3.4
3. Start at point 1 with a different number of SiPMs

Figure 4.2 shows the measurement of the time resolution versus the number of SiPMs. Two different MUSIC-boards were tested at the same time with bar 2, MUSIC-board #11 and #18. Sadly, one of the channels on board #18 broke during the test, which later on influenced the timing resolution of the whole board and had to be exchanged. Therefore there were not always enough boards to do all the test. The data was fit with the following equation:

$$f(n) = A \cdot n^B \tag{4.1}$$

A and B were the fit-parameters and n is the number of read out SiPMs. The fit was done to test the hypothesis that the the timing in the SiPMs is a statistical one, therefore the expected

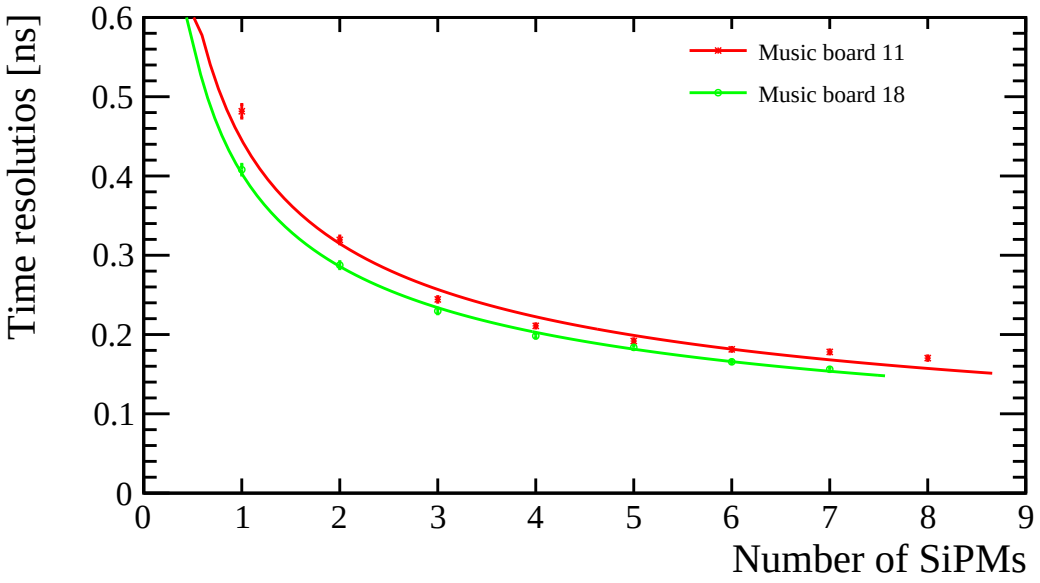

Figure 4.2: Time resolution versus number of SiPMs. The measurement was done at the test-beam with bar 2. "Music board 11" and "Music Board 18" refer to the MUSIC board number in use for the test. One SiPM is missing due to one channel of the MUSIC-board 18 not working.

value of B is expected to be -0.5. The fit result of the parameter B are listen in the table 4.1 and is consistent with $B = -0.5$.

	B
Music board 11	-0.50 ± 0.01
Music board 18	-0.50 ± 0.01

Table 4.1: Fit result of figure 4.2.

4.2.2 Amplitude Analysis

In this test, the same hypothesis as in the section before was tested. The data was not acquired by turning on a certain amount of SiPMs, but by measuring the amplitude of the signal. In the offline analysis of the test beam in June, the height of the signal could be found by scanning the waveform for their maximum, and then continue as in section 3.8. With the same data, the time resolution was calculated.

In the lab, first the amplitudes had to be collected by the scope, and afterwards the timing resolution had to be measured. Figure 4.3 shows an example of the amplitude measurement performed in the lab, in figure 4.4 is an example of a amplitude measurements of the test beam in June.

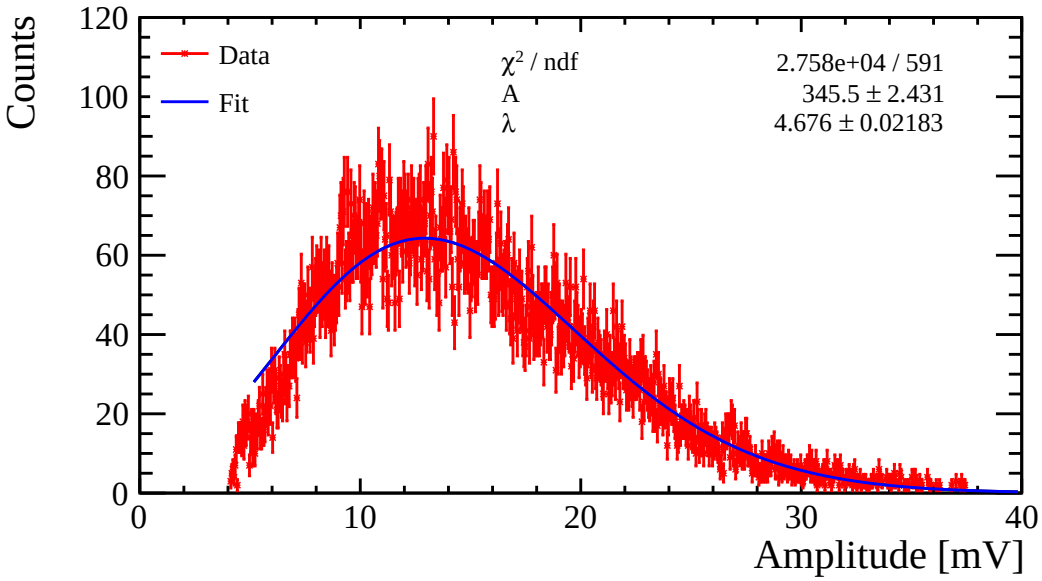

Figure 4.3: Distribution of amplitudes with e^- source of the laboratory with bar 1. The Source was 35 cm away from the SiPM array.

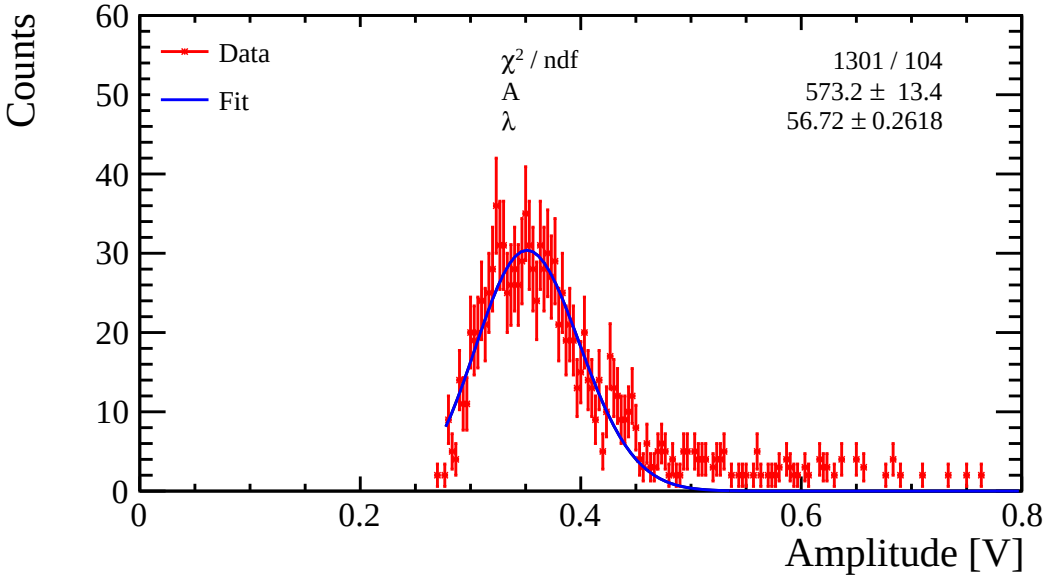

Figure 4.4: Distribution of amplitudes with beam of bar 3. The beam pointed at a spot 60 cm away from the SiPM array.

	λ	s
lab	4.67 ± 0.02	(3.1 ± 0.3) mV
beam	56.7 ± 0.3	(6.2 ± 0.6) mV

Table 4.2: The fit result of figures 4.3 and 4.4. The big differnece of s comes from the usage of the differential output during the tests at the beam.

In both cases, timing resolution and the average amount of photons were measured with bar 1, bar 2 and bar 3. The result of the measurement can be seen in figure 4.5.

The fit in figure Fig. 4.5 follows very similarly to equation 4.1:

$$f(\lambda) = A \cdot \lambda^B \tag{4.2}$$

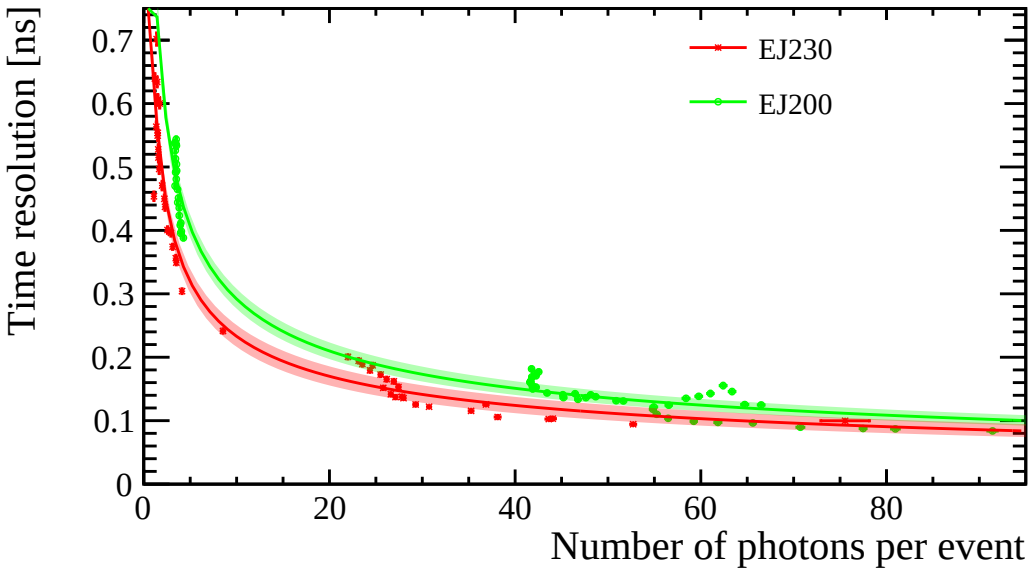

Figure 4.5: The number of Photons versus time resolution. All the bars available at the time of the test beam in June and in the lab were used. The shades are the $1\,\sigma$ errors of the fit.

where A and B are the fit parameters and λ is the number of photons. To verify the same hypothesis as in 4.2.1, the value of B is expected to be -0.5. The fit result can be seen in table 4.3 and follows reasonably $B = -0.5$. The difference comes from the correction, that was only applied in the data from the test beam, and the lower CF value in the test beam data.

	B
EJ200	-0.48 ± 0.01
EJ230	-0.45 ± 0.02

Table 4.3: Fit results of 4.5

4.2.3 Bar comparison and distance scan

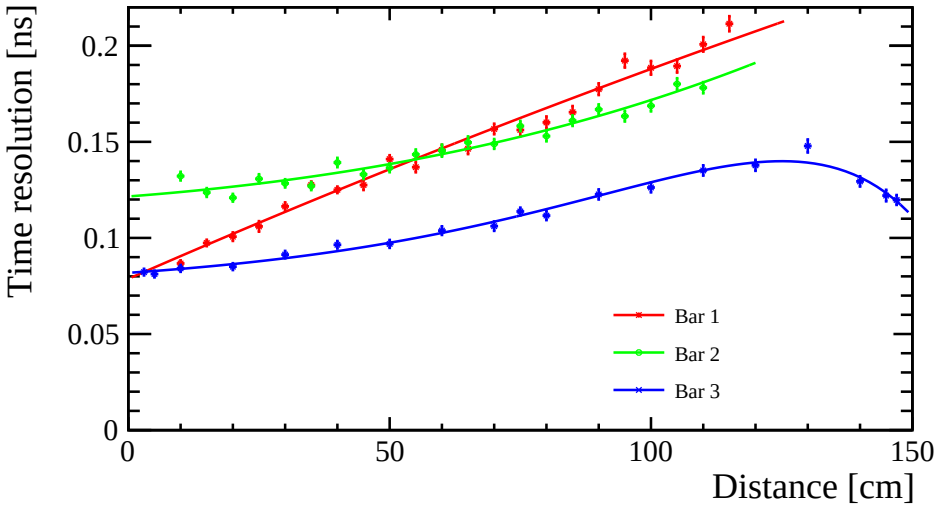

Figure 4.6: Comparison between bar 1, 2 and 3. All MUSIC-boards had the same V_{bias} of 58 V and the CF-value of 5 %. On the data the time walk correction was applied.

To measure the timing resolution over the whole distance of a bar, one point is measured and

the the bar gets moved sideways a few centimeters to a new location.

The data was fit with

$$f(x) = A \cdot e^{\alpha \cdot x} + B \cdot e^{\beta \cdot x} + C \tag{4.3}$$

Figure 4.6 shows the measured time resolution dependant of the distance between the impact point of the beam in the bar and the MUSIC-board of three different bars. It is easy to see the the bar with the smaller cross section has the better timing resolution. Also visible is, that the plastic type EJ230 has more linear behavior over the whole length of the bar as EJ200 due to its optical properties. Moreover, bar 3 may has some reflections when the impact point of the beam is near the other end of the bar due to reflections on the SiPMs. The light in the bars with larger cross section got absorbed on the plastic of the end-caps.

4.2.4 Weighted mean

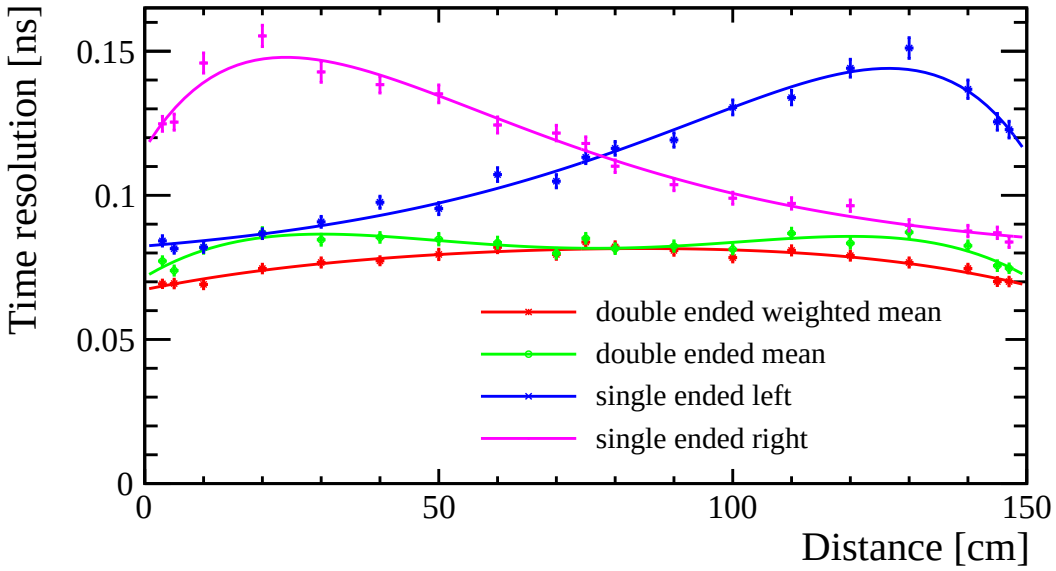

Figure 4.7: Time resolution of weighted mean of bar 3.

The fits for the single ended measurement are the same as in equation 4.3, the fit for the double ended output is as follows:

$$f(x) = A + B \cdot (x - x_m)^2 + C \cdot (x - x_m)^4 \tag{4.4}$$

A, B, and C are fit parameters and x_m is the middle point of the bar. This function is symmetric because of the assumption that both sides are equal and the bar is symmetric in time resolution.

Figure 4.7 shows the timing resolution scanned over bar 3. It had two MUSIC-boards with 8 SiPM (16 SiPMs in total) on each end for the measurement. It is easy to see that the average and the weighted mean improve the timing resolution significantly. The time resolution for a EJ200 bar with dimension 150 cm × 6 cm × 1 cm is under 100 ps over the whole bar, if the mean or the weighted mean of of the times is taken. The worst value measured was (82 ± 2) ps.

4.2.5 Different pole-zero settings of the MUSIC-board

In figure 4.8, the difference between the two PZ-settings `R3 C31` and `R5 C12` on the MUSIC-boards are shown. It was done by doing one distance scan, changing the settings on the board and repeat the scan. The data was fit according to equation 4.3.

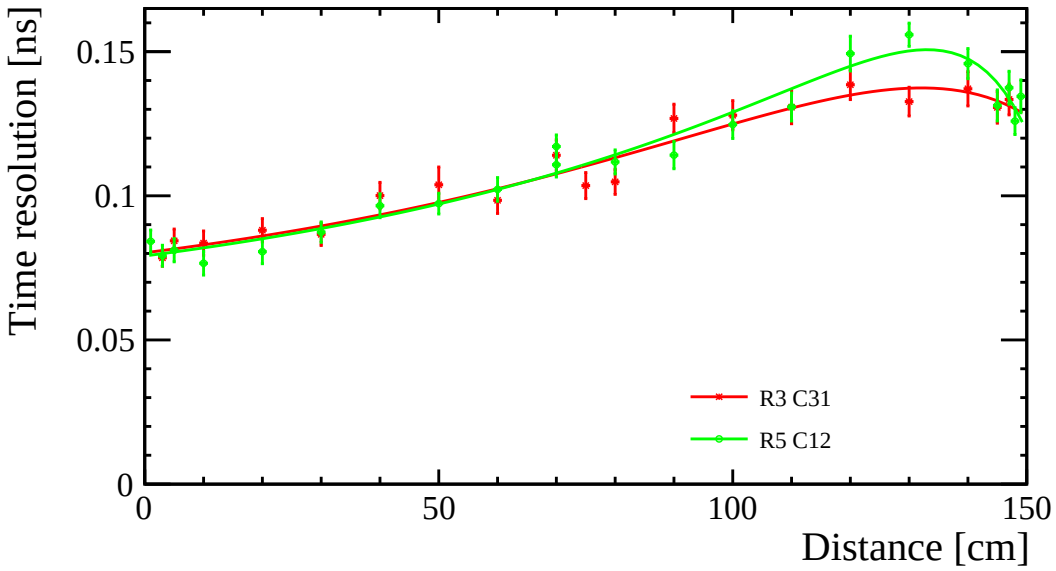

Figure 4.8: Time resolution over distance with two different zero-pole settings of the MUSIC-board on bar 3.

There is almost no effect except if the impact point is on the farther end of the bar. In that case the `R3 C31` has a timing resolution that is about 20 ps better.

4.2.6 4×2 array versus 8×1 array

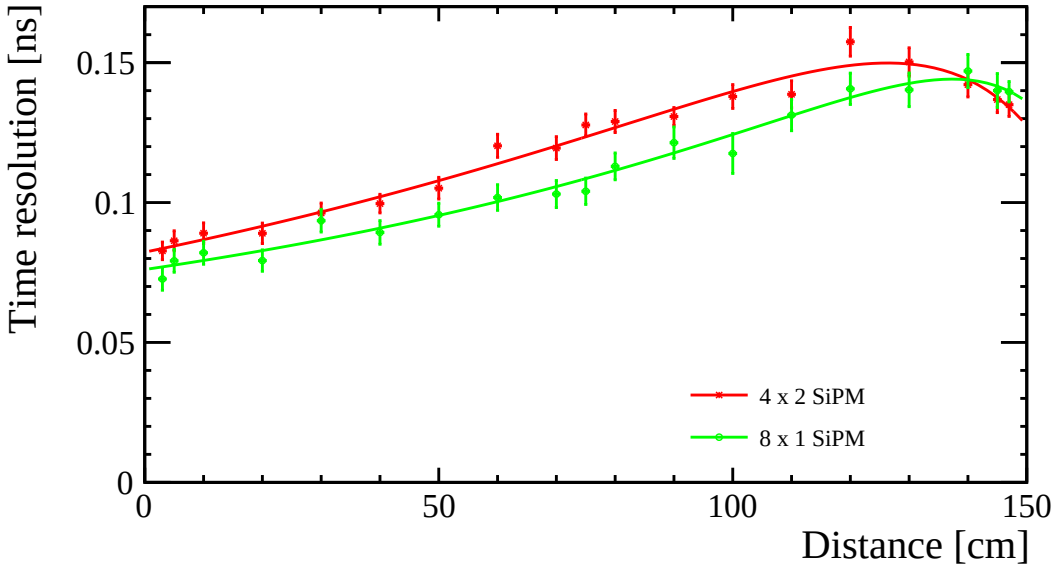

Figure 4.9: Time resolution over distance with the arrays 8×1 and 4×1 on bar 3.

Figure 4.9 shows the difference between the two different SiPM arrays on bar 3. First, the 4×2 array was tested, then swapped out for the 8×1 array. The fit function is equation 4.3. The 8×1 array had the better performance during the test and is about 15 ps better over the whole bar, due to the increased capacitance over the SiPMs in the 4×2 composition.

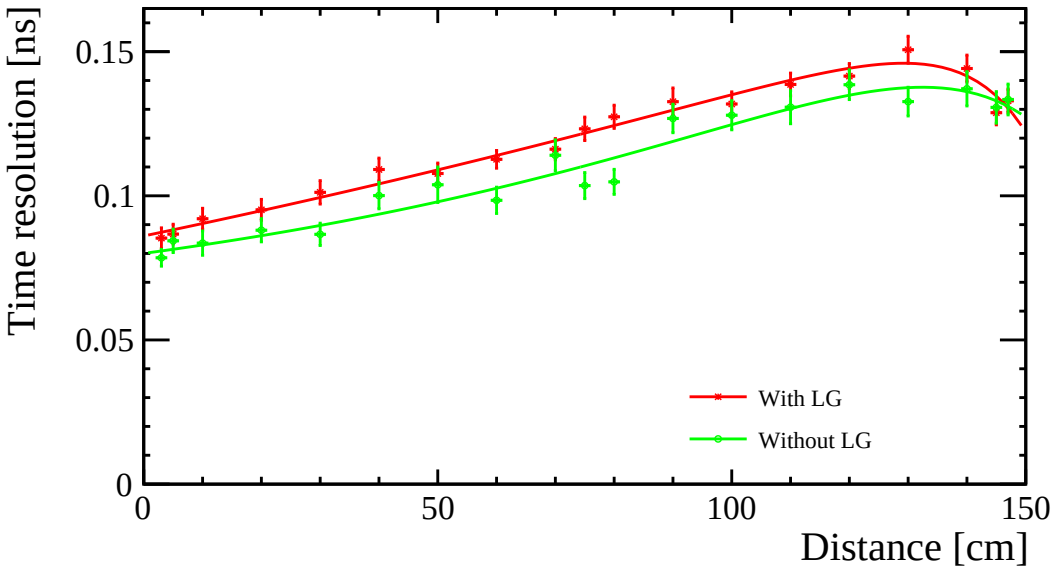

Figure 4.10: Time resolution over distance with and without Light Guide (LG) (bar 3 and 4).

4.2.7 With Light guide versus without Light Guide

Figure 4.10 shows the difference between a bar with light guide and one without. Both distance scans were done with the same board and a 8×1 array. Bars used in this test were bar 3 and bar 4.

The timing resolutions of the bar with light guides are worse due to more light being absorbed by the additional material and glue by the endcap over the light guide. In addition it is difficult to properly position a 6 mm sensor on a 6 mm tapered light guide. Focusing effect which the light guide can provide is seems to be negligible.

4.2.8 Best measurement so far

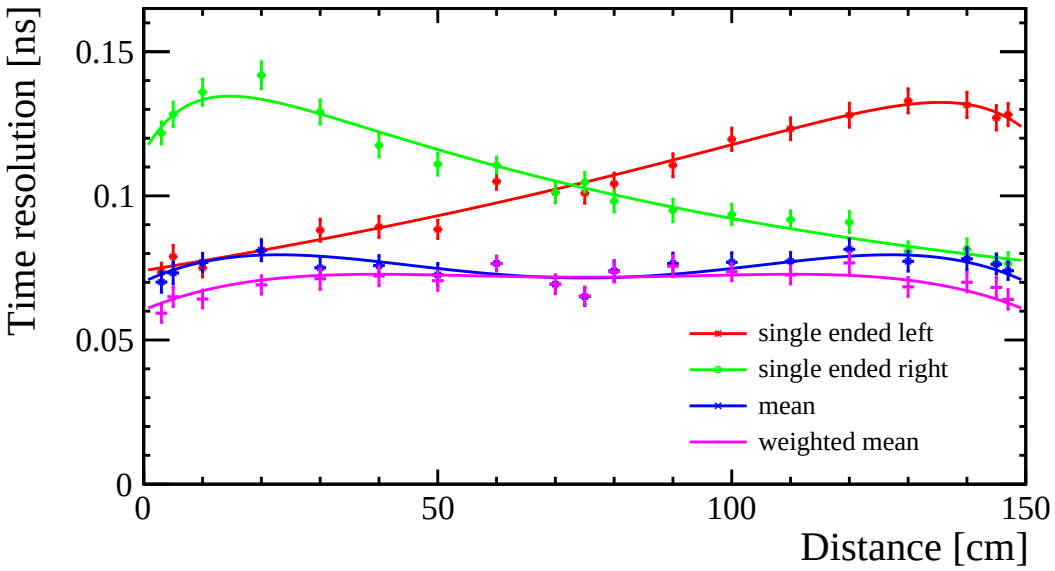

Figure 4.11: Distance scan done with an EJ200 150 cm × 6 cm × 1 cm bar without light guides (bar 3), pole zero cancellation `R3 C31`, two 8×1 arrays with bias voltage $V_{bias} = 58$ V and a a constant fraction of 5 %.

The best measurement was done in the test beam in October with bar 3. The MUSIC-boards had the pole-zero settings `R3 C31`, the SiPMs were in a 8×1 array and were biased with 58 V and the constant fraction was set to 5 %. The time resolution of the weighted mean ranges from (59 ± 3) ps to (77 ± 4) ps. The results are shown in figure 4.11.

4.3 Time of Flight measurement

As a small test in the end of the test-beam in October, a Time of Fight (ToF) measurement over a flight distance of 10 m was performed with bar 3. Both SiPM arrays on either end were of the type 8×1, and the weighted mean of both sides was taken and had the time resolution of (82 ± 2) ps for muons. The time walk correction with the correction factors of a distance scan were applied. With the time of flight, the mass squared was calculated as follows:

$$v(\Delta t) = \frac{\Delta s}{\Delta t} \tag{4.5}$$

$$\gamma(v) = \frac{1}{\sqrt{1 - v^2}} \tag{4.6}$$

$$m^2(v, p) = \frac{p^2}{\gamma^2 v^2} \Rightarrow m(\Delta s, \Delta t, p) = p\sqrt{\left(\frac{\Delta s}{\Delta t}\right)^2 - 1} \tag{4.7}$$

with the velocity v, the measured time difference between the trigger and the bar Δt, the distance Δs, the Lorenz factor γ, the momentum p and mass m.

As seen in figure 4.12, different particles are clearly visible. For the fit, normalized Gaussian were used (see equation 4.8) and the fit results can be seen in table 4.4.

$$f(m^2) = \sum_{i=1}^{n} A_i \cdot \frac{1}{\sqrt{2\pi} \cdot \sigma_i} \cdot e^{-\left(\frac{m^2 - \mu_i}{\sqrt{2} \cdot \sigma_i}\right)^2} \tag{4.8}$$

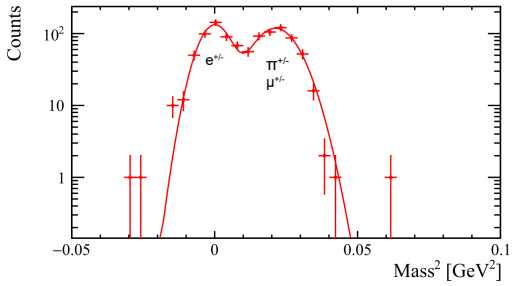

Momentum: 1 GeV.

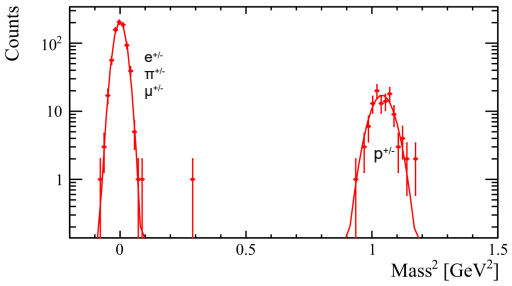

Momentum: 2 GeV.

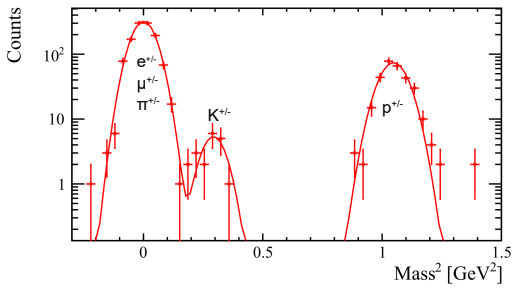

Momentum: 3 GeV.

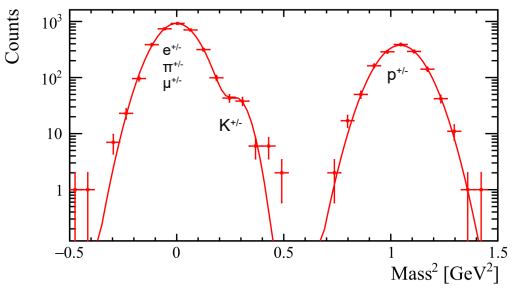

Momentum: 4 GeV.

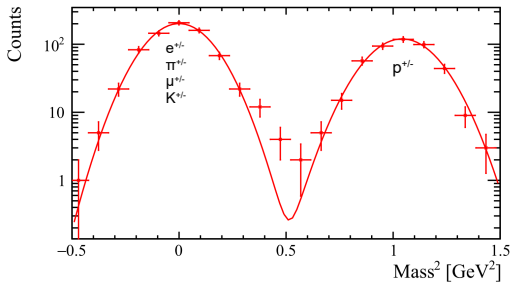

Momentum: 5 GeV.

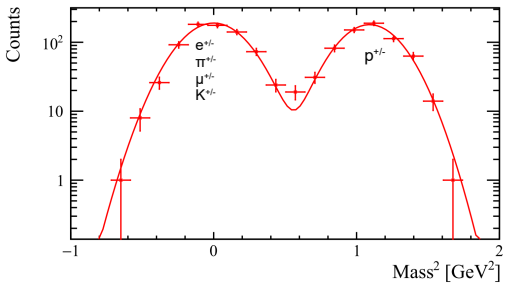

Momentum: 6 GeV.

Figure 4.12: Masses of the particles in the mixed beam calculated with equation 4.7 from the time of flight measurement with particle momentum of 1 GeV to 6 GeV with bar 3. Both arrays were 8×1,fitted with equation 4.8. The correction with the correction factors of a distance scan was applied, and the weighted mean between the two MUSIC-boards was taken. Flight distance was 10 m.

Momentum	A_i	μ_i (Mass^2)	Particles
1 GeV	1.67 ± 0.09	(0.000 ± 0.005) GeV^2	electrones
	2.14 ± 0.09	(0.021 ± 0.007) GeV^2	pions, muons
2 GeV	11.5 ± 0.2	(0.00 ± 0.02) GeV^2	electrones, muons, pions
	1.8 ± 0.3	(1.04 ± 0.04) GeV^2	protons
3 GeV	38.9 ± 0.5	(0.00 ± 0.05) GeV^2	electrones, muons, pions
	0.6 ± 0.3	(0.29 ± 0.05) GeV^2	kaons
	10.4 ± 0.5	(1.04 ± 0.05) GeV^2	protons
4 GeV	199 ± 1	(0.00 ± 0.07) GeV^2	electrones, muons, pions
	4.7 ± 0.9	(0.028 ± 0.005) GeV^2	kaons
	86 ± 1	(1.04 ± 0.09) GeV^2	protons
5 GeV	67 ± 1	(0.00 ± 0.13) GeV^2	electrones, muons, pions, kaons
	43 ± 1	(1.04 ± 0.14) GeV^2	protons
6 GeV	99 ± 3	(0.00 ± 0.21) GeV^2	electrones, muons, pions, kaons
	89 ± 3	(1.09 ± 0.20) GeV^2	protons

Table 4.4: Fits of the momentum scan. The errors on the A_i is the error of the fit and the error on the μ_i is the corresponding σ_i.

4.4 Extrapolation to longer bars

A Monte Carlo simulation was accomplished as described in section 3.9. The bar that was simulated was 170 cm long, and has the cross section of 6 cm × 1 cm. The measured points were from the the distance scan done in section 4.2.4, but one of the sides was mirrored to the other side. A few points at the far end of the MUSIC-boards were not used because the reflection effects would hinder the fit. The fit for the single-ended output is the same as in equation 4.3.

The result of the MC-simulation can be seen in figure 4.13. The mean and weighted mean are calculated according to equation 3.16 and 3.17. The shaded regions on the figure indicate the statistical errors and simulate the same amount of events as used in the extrapolation. The simulation predicts an expected time resolution for the weighted mean (73 ± 9) ps at the end of the bar and (86 ± 1) ps in the middle of a bar with dimension 170 cm × 6 cm × 1 cm and no light guides, with the SiPMs in the 8×1 configuration and the settings `R3 C31` on the MUSIC-board. This is useful because the current design of the timing detector needs bars with that dimension.

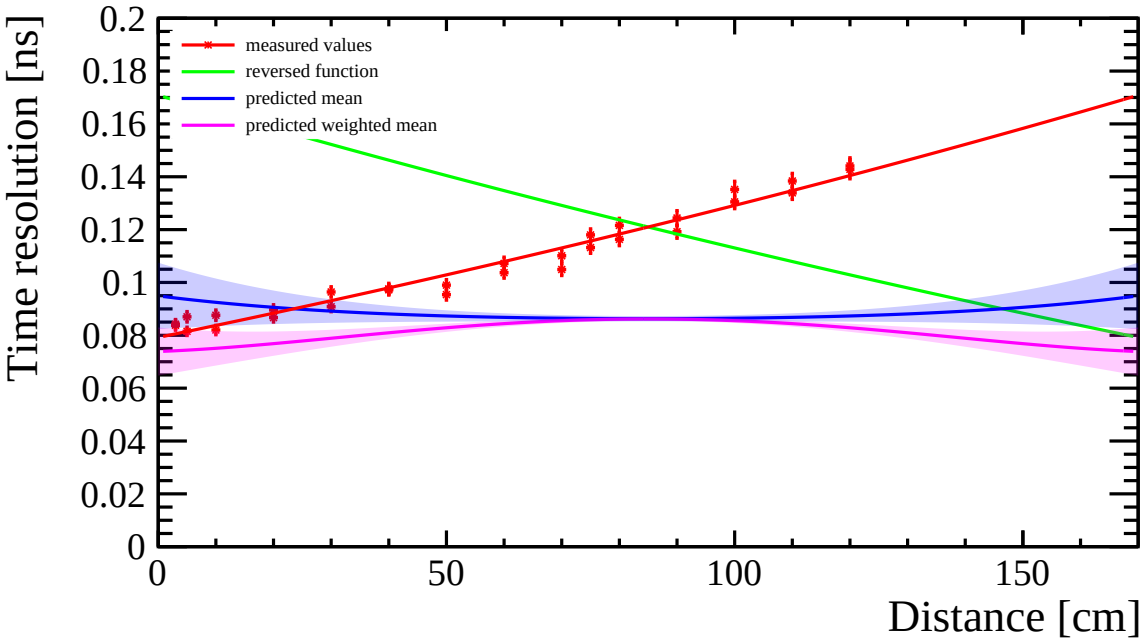

Figure 4.13: Simulated time resolution of a 170 cm × 6 cm × 1 cm bar. The Data comes from the test beam of June of bar 3, one side was flipped. The correction was applied. The Errors (shaded region) is statistical, the Simulation was done with as many events as there where in measurements. The formula of the fit is as in equation 4.4.

5 Summary and Outlook

SHiP is a proposed fixed target experiment at the CERN SPS-accelerator. It's goal is to search for new physics beyond the standard model by dumping a 400 GeV proton beam on a heavy target. This method requires a sophisticated concept to get rid of a massive muon-background. The sweeping magnet directly downstream of the target should deflect most of the muons from the proton-proton interaction in the target. Backscattering, cosmic muons and products from neutrino-interaction will cause a large combinatorial di-muon background and fake signals in the decay-volume. Therefore, a dedicated veto-timing detector with a timing resolution better than 100 ps must be installed between the vacuum vessel and the calorimeters to classify di-muon events either as signal or background. One of the options for such a veto-timing detector is a setup with scintillator bars read out by SiPMs.

This thesis tested different scintillating bars with 8 SiPMs mounted on MUSIC-boards on either side. Bars were tested in the laboratory in Zürich with a ^{90}Sr source and in June 2017 at the T9 test facility at CERN. In October of the same year, a comparison between a bar without light guides and a bar with light guides was measured at the same location at CERN. Moreover, two different SiPM arrays and two different settings on the MUSIC-board were examined during that test beam. The best time resolution were achieved with a EJ200 bar with dimension 150 cm × 6 cm × 1 cm without light guides. The timing resolution is (77 ± 4) ps in a muon beam with momenta from 1 GeV to 6 GeV. Furthermore the assumption that the time resolution is a statistical process, i.e. $\sigma \propto 1/\sqrt{N}$ (N is the number of photons per event), was tested and confirmed. Moreover, a simple simulation extrapolated the timing resolution for a bar with dimension 170 cm × 6 cm × 1 cm of the type EJ200. The simulated time resolution is (86 ± 1) ps, and is therefore still better than the necessary time resolution of 100 ps for the timing detector of SHiP.

As a next step towards the timing detector, a prototype with 22 scintillator bars without light guides will be constructed by June 2018. The scintillators will be made out of the EJ200 plastic and will have the dimension 168 cm × 6 cm × 1 cm, as the planned size for the timing detector at SHiP. The prototype will have a total of 44 mini-MUSIC boards (currently under development) and 352 SiPMs. The 44 channels will be recorded by a 48 channel *SAMPIC* digitizer.

A Additional information about devices

A.1 Characterization of the Hamamatsu *S13360-6050PE*

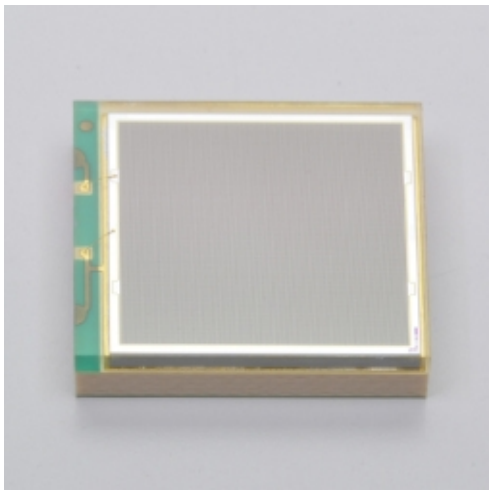

Figure A.1: Sipm Of the type Hamamatsu *HPK-S13360-6050PE*. [38]

Photosensitve area	6 mm × 6 mm
Pixel pitch	50 μm
Number of pixels	14400
Spectral response range	320 nm to 900 nm
Peak sensitivity	450 nm
Dark count (producer)	2000 kHz
Dark count (meausured) [31][6]	2800 kHz
Gain	$1.7 \cdot 10^6$
Typical BdV	52 V
Recommended Operating Voltage	BdV+3 V
Cross talk [31][6]	4.5 %
Recovery time	32.85 ns

Table A.1: All data from [38] except when stated otherwise. Everything is for the recommended operating voltage and a temperature of 25 °C.

[6]This value was measured with the Hamamatsu *HPK-S13360-3050CS*, which is the 3 mm × 3 mm version of the *HPK-S13360-6050PE*.

A.2 Trigger board

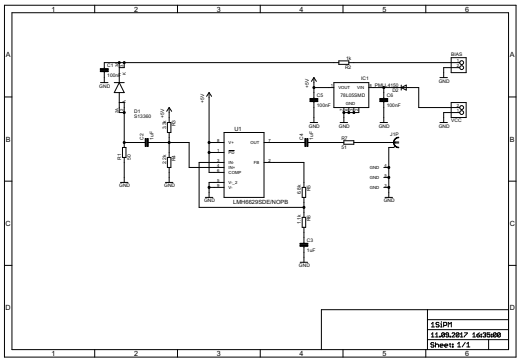

Figure A.2: Circuit diagram of the trigger board

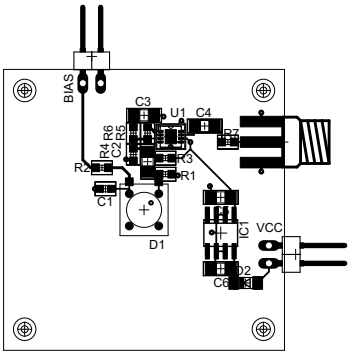

Figure A.3: Trigger board layout

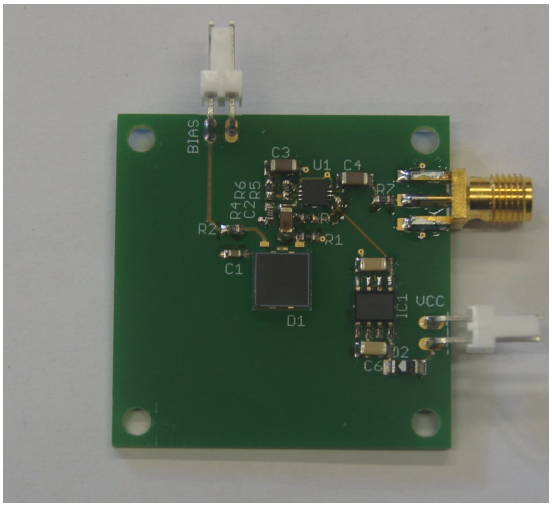

Figure A.4: Front view of the assambled trigger board.

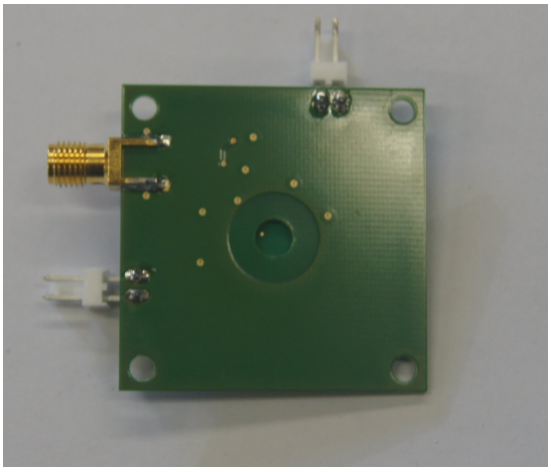

Figure A.5: The trigger board from the back. Notice the hole in the middle, so that the electrones have less material to pass through before they get into the scintillator

A.3 Dark box schematics

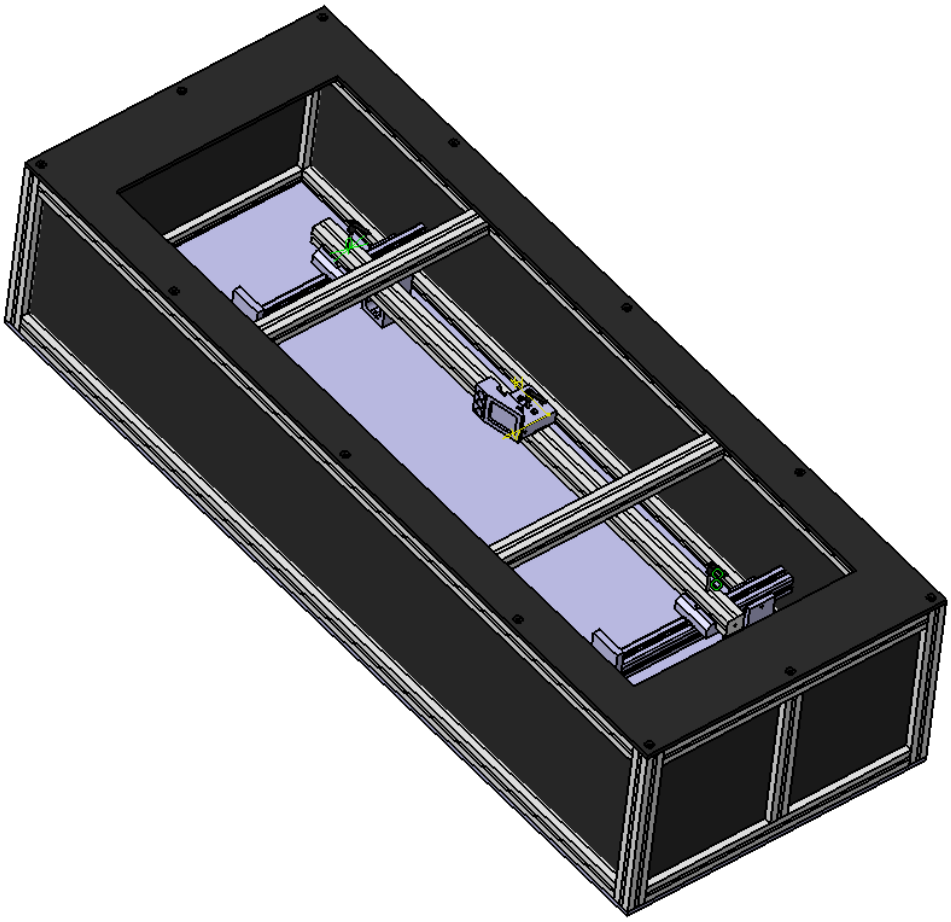

Figure A.6: The Dark box from the outside. [31]

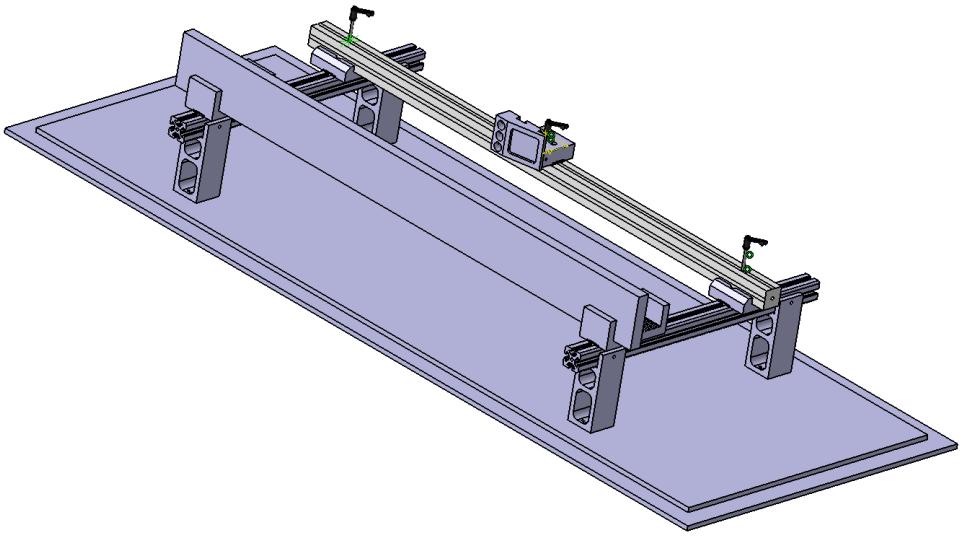

Figure A.7: The insides of the dark box from. [31]

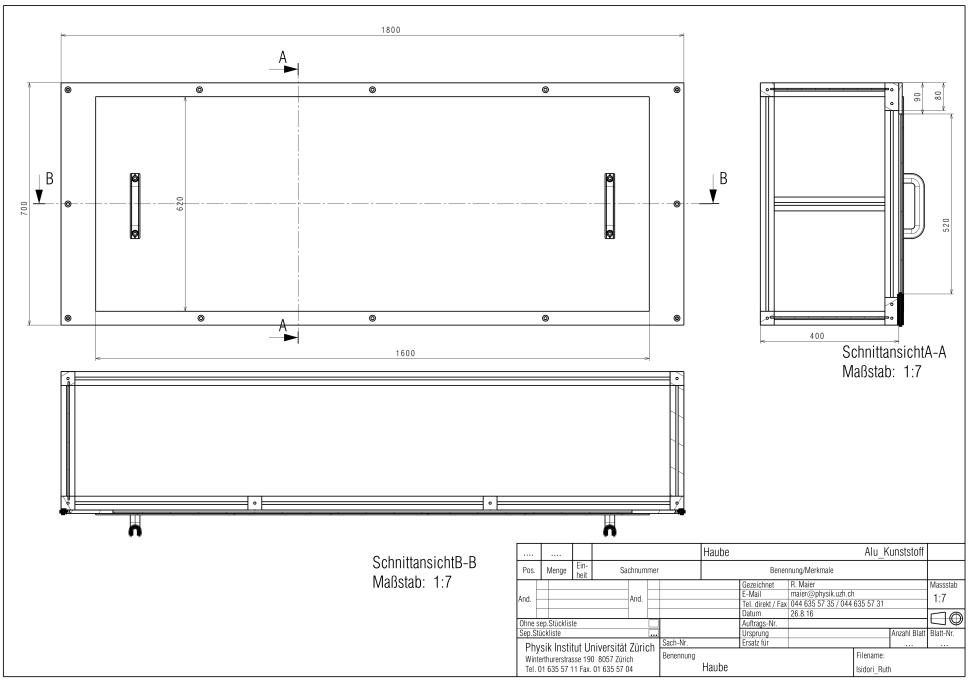

Figure A.8: The Dark box schematics. [31]

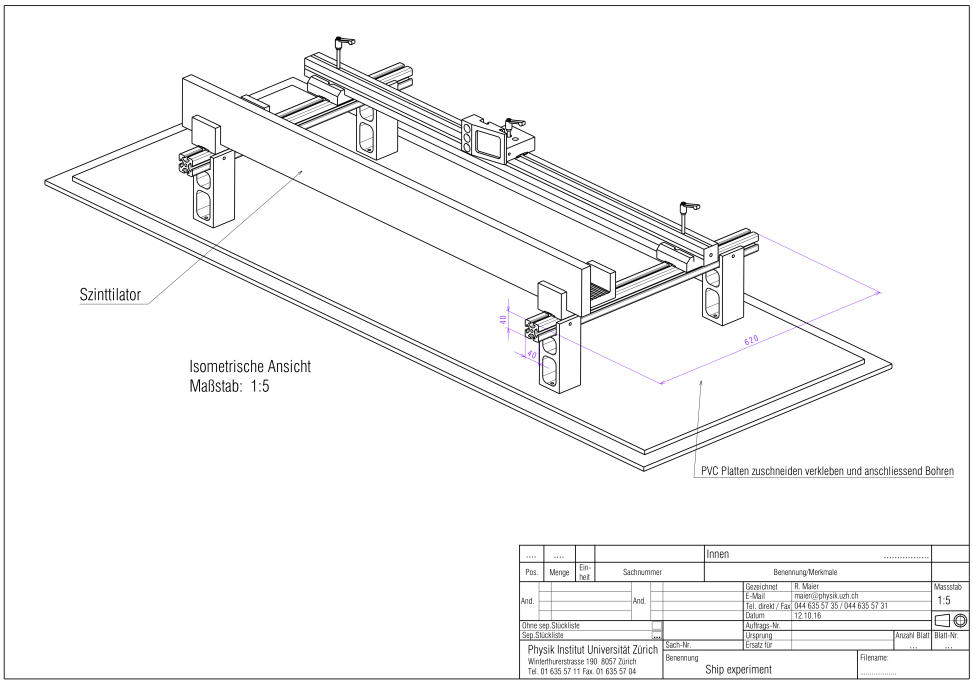

Figure A.9: Schematics of the railings inside the box. [31]

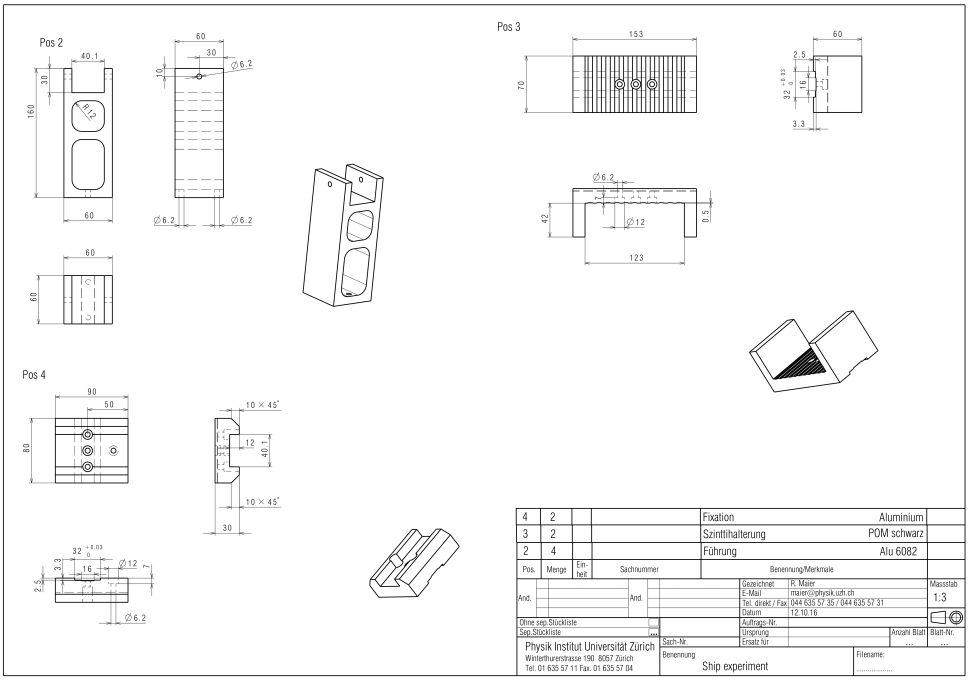

Figure A.10: Schematics of the parts to hold railings and scintillator in place. [31]

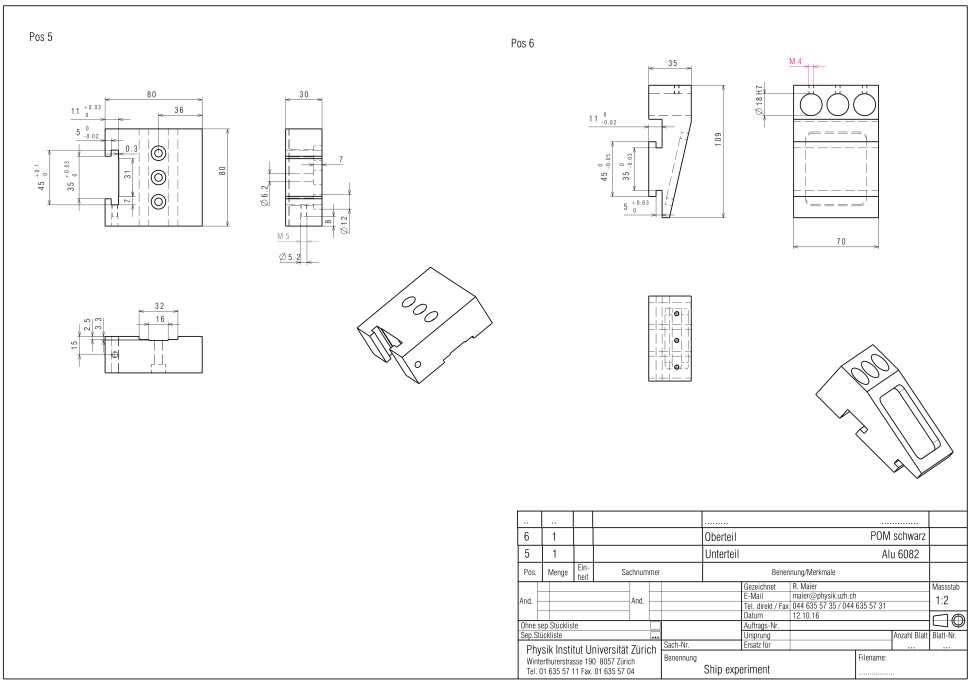

Figure A.11: Schematics of the railings inside the box. [31]

B Additional Graphs

B.1 Effect of the time walk correction

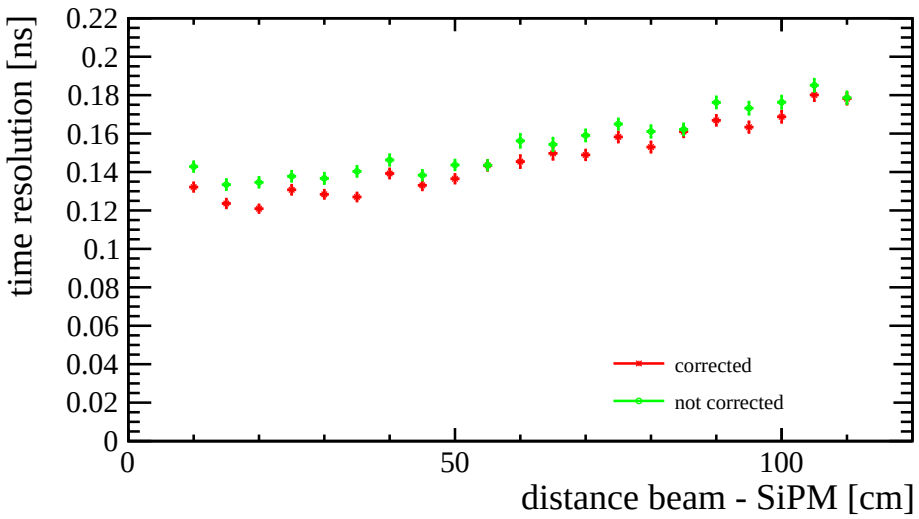

Figure B.1: Comparison with and without corrections,bar 2.

B.2 Time of Flight measurement

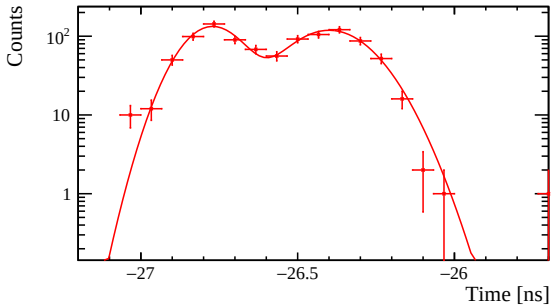

Momentum: 1 GeV.

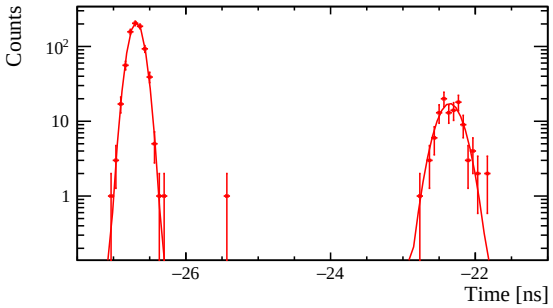

Momentum: 2 GeV.

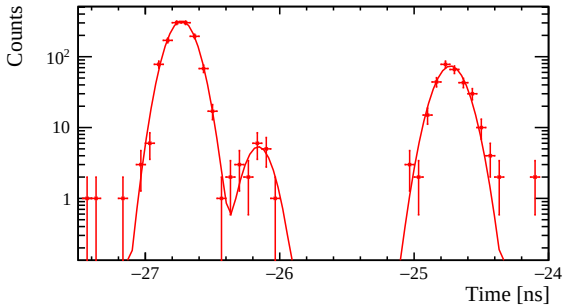

Momentum: 3 GeV.

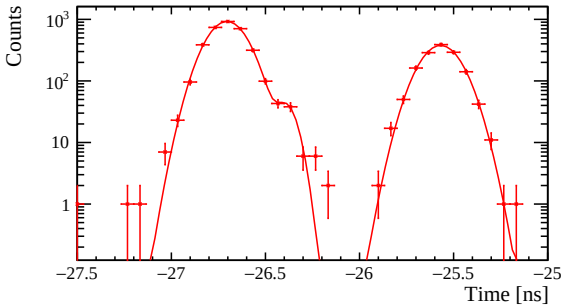

Momentum: 4 GeV.

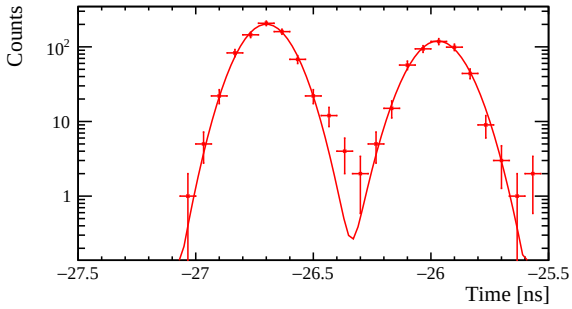

Momentum: 5 GeV.

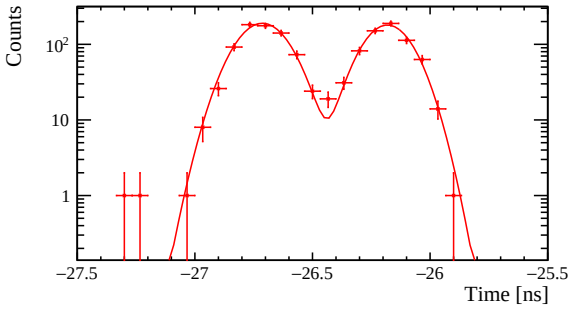

Momentum: 6 GeV.

Figure B.2: Time measured in the ToF measurement with flight distance 10.6 m.

Acknowledgements

I would like to thank Prof. Nicola Serra for the opportunity to test and optimize the timing detector as part of the SHiP group Zürich and giving me a chance for an in-depth look into the development of a new experiment. I thank also the SHiP timing group for including me in their team and helping me out if needed.

A very special thanks goes to Dr. Christopher Betancourt for his support as supervisor. His advice was always very help-full, and he also gave me the chance to get some responsibilities on my own.

Furthermore, I want to thank Ruth Bründler for teaching me the basics of the timing detector and helping me out at the measurements at CERN. I also want to thank Dr. Alexander Korzenev and Dr. Barbara Storacci for the help at the test-beams and in the bureaucracy of CERN.

I want to thank Sergio Gomez and his group for developing the MUSIC-board and helping me when technical difficulties have arisen with the board.

Moreover, I'd like to thank Dr Achim Vollhard for developping the the trigger board and Reto Maier for constructing the mechanical support of the experiment.

References

[1] SHiP Collaboration. *Addendum to Technical Proposal: A Facility to Search for Hidden Particles (SHiP) at the CERN SPS*. Tech. rep. CERN-SPSC-2015-040. SPSC-P-350-ADD-2. Geneva: CERN, Oct. 2015. URL: http://cds.cern.ch/record/2060742.

[2] Georges Aad et al. "Observation of a new particle in the search for the Standard Model Higgs boson with the ATLAS detector at the LHC". In: *Physics Letters B* 716.1 (2012), pp. 1–29.

[3] S. Chatrchyan et al. "Observation of a new boson at a mass of 125 GeV with the CMS experiment at the LHC". In: *Physics Letters B* 716.1 (2012), pp. 30–61. ISSN: 0370-2693. DOI: https://doi.org/10.1016/j.physletb.2012.08.021. URL: http://www.sciencedirect.com/science/article/pii/S0370269312008581.

[4] Joan Elias-Miró et al. "Higgs mass implications on the stability of the electroweak vacuum". In: *Physics Letters B* 709.3 (2012), pp. 222–228. ISSN: 0370-2693. DOI: https://doi.org/10.1016/j.physletb.2012.02.013. URL: http://www.sciencedirect.com/science/article/pii/S037026931200144X.

[5] Elena Graverini. *SHiP sensitivity to Heavy Neutral Leptons*. Tech. rep. 2016. URL: http://cds.cern.ch/record/2214085/files/ship-note-hnls.pdf.

[6] Peter W Graham, David E Kaplan, and Surjeet Rajendran. "Cosmological relaxation of the electroweak scale". In: *Physical review letters* 115.22 (2015), p. 221801.

[7] Gaia Lanfranchi. "Sensitivity of the SHiP experiment to a light scalar particle mixing with the Higgs". In: (Jan. 2017). URL: http://cds.cern.ch/record/2243034.

[8] SN Gninenko, DS Gorbunov, and ME Shaposhnikov. "Search for GeV-scale sterile neutrinos responsible for active neutrino oscillations and baryon asymmetry of the Universe". In: *Advances in High Energy Physics* 2012 (2012).

[9] Dmitry Gorbunov and Mikhail Shaposhnikov. "How to find neutral leptons of the νMSM?" In: *Journal of High Energy Physics* 2007.10 (2007), p. 015. URL: http://stacks.iop.org/1126-6708/2007/i=10/a=015.

[10] M. Anelli et al. "A facility to Search for Hidden Particles (SHiP) at the CERN SPS". In: (2015). arXiv: 1504.04956 [physics.ins-det].

[11] SHiP collaboration. *facility_acc_complex.png*. 2015. URL: https://cds.cern.ch/record/2030193/files/facility_acc_complex_image.png?subformat= (visited on 12/07/2017).

[12] SPS CERN and PS Experiments Comittee (SPSC). *Minutes of the 120 the Meeting of the SPSC Held on Tuesday 19 January and Wednesday 20 January 2016*. 2016. URL: http://ship.web.cern.ch/ship/Constitution/Minutes/CRB-minutes-10feb2016.pdf (visited on 12/07/2017).

[13] M. Calvian. "Status of BDF/SHiP target and target complex (TTC) studies". In: *11. SHiP Collaboration Meeting*. 2017. URL: https://indico.cern.ch/event/638036/contributions/2593440/attachments/1471589/2277517/mc__BDF_TTC_SHiP_CM_June2017_v1.3.pdf.

[14] A. Akmete et al. "The active muon shield in the SHiP experiment". In: *Journal of Instrumentation* 12.05 (2017), P05011. URL: http://stacks.iop.org/1748-0221/12/i=05/a=P05011.

[15] Giovanni De Lellis. "The neutrino/LDM detector: towards the CDS and beyond". In: *11. SHiP Collaboration Meeting*. 2017. URL: https://indico.cern.ch/event/638036/contributions/2593469/attachments/1472082/2280653/Neutrino_GDL.pdf.

[16] Andrea Prota. "Structural aspects related to the vacuum vessel of the SHIP Project". In: *10. SHiP Collaboration Meeting*. 2017. URL: https://indico.cern.ch/event/638036/contributions/2593468/attachments/1472130/2278447/CERN_07_giugno_2017_Prota.pdf.

[17] Heiko Lacker. "SBT News from LiquidScintillator detector development". In: *11. SHiP Collaboration Meeting*. 2017. URL: https://indico.cern.ch/event/578880/contributions/2439457/attachments/1409870/2156430/sbt-status-feb2017.pdf.

[18] Rainer Wanke. "Thoughts about an alternative ECAL Layout". In: *11. SHiP Collaboration Meeting*. 2017. URL: https://indico.cern.ch/event/638036/contributions/2593487/attachments/1472009/2278226/ECAL_CollabMeeting_Jun17.pdf.

[19] W. Baldini et al. "Measurement of parameters of scintillating bars with wavelength-shifting fibres and silicon photomultiplier readout for the SHiP Muon Detector". In: *Journal of Instrumentation* 12.03 (2017), P03005. URL: http://stacks.iop.org/1748-0221/12/i=03/a=P03005.

[20] N Abgrall et al. "NA61/SHINE facility at the CERN SPS: beams and detector system". In: *Journal of Instrumentation* 9.06 (2014), P06005. URL: http://stacks.iop.org/1748-0221/9/i=06/a=P06005.

[21] Hamamatsu Photonics. *MPPC and MPPC module for precision measurement*. 2016. URL: http://www.hamamatsu.com/resources/pdf/ssd/mppc_kapd0004e.pdf (visited on 12/13/2017).

[22] Olaf Steinkamp. *Lecture Notes: Experimental Methods of Particle Physics(PHY461), Silicon detectors*. Nov. 2017. URL: http://www.physik.uzh.ch/dam/jcr:1dab7b67-a936-41a2-939a-abb508df5b4f/empp17_OS_silicon.pdf.

[23] Nicoleta Dinu. "Characteristics of the Silicon PhotoMultiplier (SiPM) detectors". In: Dec. 2006.

[24] Nepomuk Otte. "The silicon photomultiplier-a new device for high energy physics, astroparticle physics, industrial and medical applications". In: *Proceedings to SNIC symposium (SLAC, Stanford, 2006)*. 2006.

[25] Hamamatsu Corporation Slawomir Piatek and New Jersey Institute of Technology. *A technical guide to silocon photomultipliers (SiPM)*. 2017. URL: https://www.hamamatsu.com/us/en/community/optical_sensors/articles/technical_guide_to_silicon_photomultipliers_sipm/index.html (visited on 12/13/2017).

[26] P Eckert, R Stamen, and H -C Schultz-Coulon. "Study of the response and photon-counting resolution of silicon photomultipliers using a generic simulation framework". In: *Journal of Instrumentation* 7.08 (2012), P08011. URL: http://stacks.iop.org/1748-0221/7/i=08/a=P08011.

[27] S. Gomez et al. "MUSIC: An 8 channel readout ASIC for SiPM arrays". In: *Proceedings, Optical Sensing and Detection IV*. 2016.

[28] University of Barcelona. *MUSICR1: 8 channel Multiple Use IC for SiPM anode readout, board description*. 3.1. 2017. URL: http://siub.ub.edu/downloads/music/.

[29] University of Barcelona. *MUSICR1: 8 channel Multiple Use IC for SiPM anode readout, software manual*. 2.2. 2017. URL: http://siub.ub.edu/downloads/music/.

[30] University of Barcelona. *MUSICR1: 8 channel Multiple Use IC for SiPM anode readout, Data Sheet*. 2017. URL: http://siub.ub.edu/downloads/music/.

[31] R. Bründler. "SiPM Readout for SHiP Timing Detector". Supervised by Dr. C. Betancourt and Prof. Dr. Nicola Serra. Masterthesis. University of Zurich, Apr. 2017.

[32] Eljen Technology. *General purpose plastic scinitllator, EJ-200, EJ-204, EJ-208, EJ-212*. 2018. URL: http://www.eljentechnology.com/images/products/data_sheets/EJ-200_EJ-204_EJ-208_EJ-212.pdf (visited on 01/24/2018).

[33] Eljen Technology. *Fast timing plastic scinitllator, EJ-228, EJ-230*. 2018. URL: http://www.eljentechnology.com/images/products/data_sheets/EJ-228_EJ-230.pdf (visited on 01/24/2018).

[34] D. Breton et al. "The WaveCatcher family of SCA-based 12-bit 3.2-GS/s fast digitizers". In: *2014 19th IEEE-NPSS Real Time Conference*. May 2014, pp. 1–8. DOI: 10.1109/RTC.2014.7097545. URL: http://ieeexplore.ieee.org/abstract/document/7097545/.

[35] C. Betancourt et al. "Application of large area SiPMs for the readout of a plastic scintillator based timing detector". In: *Journal of Instrumentation* 12.11 (2017), P11023. URL: http://stacks.iop.org/1748-0221/12/i=11/a=P11023.

[36] N Cartiglia et al. "Performance of ultra-fast silicon detectors". In: *Journal of instrumentation* 9.02 (2014), p. C02001. URL: https://arxiv.org/pdf/1312.1080.pdf.

[37] A Blondel et al. “Study of timing characteristics of a 3 m long plastic scintillator counter using waveform digitizers”. In: *Nuclear Instruments and Methods in Physics Research Section A: Accelerators, Spectrometers, Detectors and Associated Equipment* 877 (2018), pp. 9–15.

[38] Hamamatsu. *MPPC S13360-6050PE , Hamamatsu Photonics*. 2016. URL: http://www.hamamatsu.com/jp/en/S13360-6050PE.html (visited on 12/15/2017).